SOLUTION MINING RESEARCH INSTITUTE

679 Plank Road
Clifton Park, NY 12065, USA

www.solutionmining.org
Telephone: +1 518 579 6587

Technical Conference Paper

Technical Conference Paper

Airengy Compressed Air Power Plant (CAPP) Site Selection, Considerations, and Updates

Dror Tapiero
Airengy, Ra'anana, Israel

Tzvi Joshua
Airengy, Ra'anana, Israel

Tjeerd Koopmans
Mole Underground projects & Consultancy, Utrecht, the Netherlands

Bruno Colcombet
Geostock, Rueil-Malmaison, France

PhD. Or Yogev
Airengy, Ra'anana, Israel

Solution Mining Research Institute

Spring 2026

Technical Conference

Edinburgh, Scotland, 26 – 28 April 2026

Airengy Compressed Air Power Plant (CAPP) Site Selection, Considerations, and Updates

D. Tapiero[a,1], T. Joshua[a], T. Koopmans[b], B. Colcombet[c], O. Yogev[a]

[a] Airengy, 8 Ha'Pnina st. REIT1 Building, Ra'anana, 4321545, Israel

[b] Mole Underground projects & consultancy, Utrecht, the Netherlands

[c] Geostock, Rueil-Malmaison, France

[1] Corresponding author. Airengy, 8 Ha'Pnina st. REIT1 Building, Ra'anana, 4321545, Israel
E-mail address: dror.tapiero@airengy.com

Abstract

This paper presents technical and commercial updates regarding Compressed Air Power Plant (CAPP) system, developed by Airengy (formerly Augwind). The system delivers isothermal compressed air energy storage (I-CAES) by integrating solution-mined salt caverns with isothermal compression and expansion technology (AirBattery). The paper follows O. Yogev et al.: "Isothermal Compressed Air Energy Storage (I-CAES) in Solution Mined Salt Cavern". It covers certain implementation considerations, with an emphasis on a specific project under evaluation with Kistos Energy Storage in the UK.

The CAPP concept provides dispatchable energy storage for long-durations days and weeks. Such dispatchable assets are highly needed in markets with a high share of solar and wind generation, to address multi-day scarcity events, and energy curtailment.

Three technical advances made at the AirBattery demonstrator are presented. First, the expedition of the isothermal process, resulting in improved power density (in terms of land and environmental footprint as well as capex reduction). Second, integration of lithium-ion battery energy storage system (BESS), resulting in a high-quality power profile and black start capability. Third, the facility transitioned to completely autonomous operation and is fully remotely controlled.

The paper details key considerations related to CAES implementation as well as site selection criteria. An in-depth look is provided into the Kistos Energy Storage Hilltop cavern field in the UK. The field features narrow salt pillars between caverns and several natural gas storage caverns. Based on a geo-mechanical assessment performed by Geostock, two brine-filled hydraulically connected caverns are identified as the preferred candidates for CAES conversion, due to their distance from natural-gas storage caverns. The assessment recommended an operating pressure window of 31–37.5 bar gauge, bounded by roof stability as well as pressure differentials from adjacent brine-filled caverns. The caverns combined geometric volume is 1.3 million m³, yielding a theoretical maximum isothermal work of 847 MWh at the recommended operating pressure window.

The paper further explores the effect of well-related pressure losses on compressed air energy losses. It illustrates that energy losses (expressed as share of initial energy) are substantially smaller than pressure losses (expressed as share of initial pressure). For the assessed case, dual-well operation through 5-1/2″ strings would result in acceptable losses (below 0.5 bar at design flow rates). Finally, the debrining strategy for the hydraulically connected caverns is considered, with an emphasis on pressure-equalization requirements.

Key words: compressed air energy storage, CAES, isothermal, liquid piston, salt cavern, long-duration energy storage, LDES, BESS hybridization, wellhead pressure loss, compressible flow, debrining, site selection

NOMENCLAURE

A_c	Cross-sectional pipe area	m^2	***Subscripts***	
a	Mechanical energy loss coefficient	$Pa^2\ m^{-1}$	0	Atmospheric / normal conditions
b	Hydrostatic forces coefficient	m^{-1}	act	Actual case
C	Pressure-volume product	$Pa\,m^3$	air	Air
d_{in}	Internal pipe diameter	m	BESS	Battery energy storage system
ΔE	Energy change	kWh	blower	Blower
Δp	Pressure change	bar	bubble	Air bubble transferred per cycle
E_{loss}	Energy loss	%	cavern	Cavern
$\bar{f}$	Average friction factor	-	ch	Charging
g	Gravitational acceleration	$m\ sec^{-2}$	closed	Closed-valve isothermal expansion phase
H	Head loss	m	dis	Discharging
K_Σ	Cumulative loss coefficient for fittings distributed along length	-	exp	Grid export
L	Pipeline length	m	f	Final expanded state
m	Mass	kg	gravity	Hydrostatic elevation component
$\dot{m}$	Mass flow rate	$kg\ sec^{-1}$	grid	Grid
p	Pressure	bar	ideal	Ideal case
P	Power	kW	imp	Grid import
Q_0	Normal volumetric flow rate	$Nm^3\ day^{-1}$	in	Pipeline inlet
R_{air}	Gas constant for air = 287	$J\ (kg\ K)^{-1}$	j	Case index
T	Temperature	K	loss	Frictional and localized resistance component
T_0	Temperature at normal conditions	K	max	Maximum
t	Time	sec	min	Minimum
v	Fluid velocity	m/sec	open	Open-valve constant-pressure phase
V	Volume	m^3	out	Pipeline outlet
W	Work	MWh	pump	Hydraulic pump
x	Spatial coordinate in the flow direction	m	set	Cycle-average setpoint
z	Depth	m	tot	Total
Greak Symbols			turb	Hydraulic turbine
η	Efficiency	-	wh	Wellhead
θ	Flow direction angle	$^\circ\ or\ rad$		
ρ	Fluid density	$kg\ m^{-3}$		
σ_v	Vertical stress in the salt pillars	MPa		
τ	Cycle duration	sec		

Table of Contents

1. Introduction

1.1 The need for flexibility

Global power demand continues to rise rapidly as the age of electricity gathers pace, supported by the increasing electrification of industry, transportation, and the buildings sectors. Growing consumption is also coming from some of the most dynamic segments of global economies, such as artificial intelligence (AI), data centers, and evolving technological innovations. As electricity use grows, power systems will need greater flexibility to securely and cost-effectively integrate an increasingly diverse mix of electricity generation sources while accommodating evolving demand patterns and technologies. [1]

Demand for electricity continues to rise, and intermittent renewable power sources (photovoltaic solar and wind) are gaining dominance in many geographies. Key drivers for the increased share of renewable generation have been (1) technological and cost improvements (2) emissions related policies, such as carbon taxation. Recent geopolitical conflicts in Eastern Europe and the Middle East further emboldened energy independence considerations, strengthening the need to reduce imported fuel reliance. Increased penetration of renewables is featured by periods of oversupply, and very low wholesale prices. Conventional power plants cannot cover their fuel and carbon costs during those hours. This reduces conventional power plants potential operating hours ("load-factor") and economic viability. Another feature of increased renewable energy sources is curtailment due to congestion in transmission grids. Transmission grids do not always have the capacity to send the electric supply from remote regions (such as the North Sea) to demand areas. Substantial amounts of energy are curtailed and wasted due to lack of transmission capacity [2,3].

In high-renewable power systems, curtailment increasingly emerges as a structural outcome of the combined effects of (1) temporal mismatch between VRE production and load, and (2) transmission constraints that prevent the evacuation of low-marginal-cost generation from high-yield regions into demand centers. Under these conditions, periods occur in which the system experiences excess renewable production, resulting in either forced renewable curtailment or negative and near-zero electricity prices. These events are more prevalent during spring and summer months but are also observed throughout the year. Similarly, when VRE production is low, wholesale prices tend to spike, as the marginal price is set by seldom used and less efficient conventional power plants.

A representative example is shown in Fig. 1, tracking renewable generation share (left axis) and hourly wholesale prices (right axis) in Germany during late 2024. For a period of 10 days between November 3rd and November 13th, generation from solar and wind sources was 70% lower than annual average. Such events of low VRE are also called "Dunkelflaute" in German. Similar underproduction occurred in neighboring markets, resulting in sustained periods of extremely high electricity prices across Central Europe and the UK. German hourly wholesale prices surged above 800 €/MWh, indicating substantial scarcity. This behavior highlights that the limiting case for storage is not merely intraday shifting, but rather multi-day energy adequacy under correlated renewable scarcity. This was further illustrated by the subsequent December 2024 event in Fig. 1, during which wholesale prices exceeded 900 €/MWh. In contrast, between these two events, on November 24th and 25th of 2024, wholesale prices remained under 17 €/MWh for a consecutive period of 31 hours.

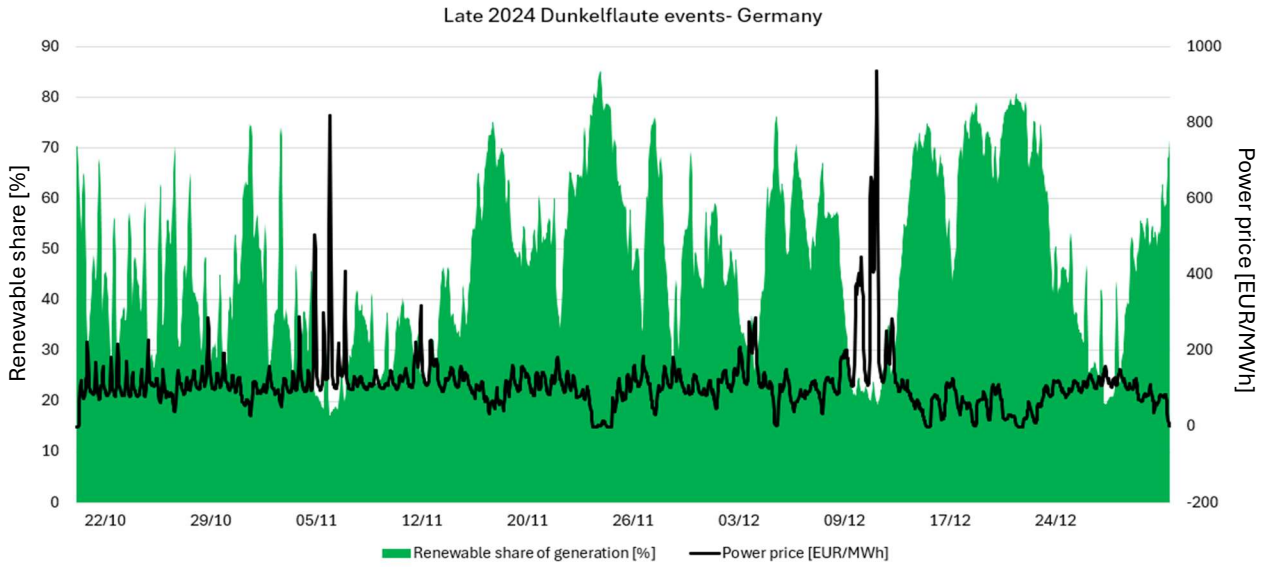

Figure 1. German Price Dynamics in Late 2024 [4]

From the perspective of energy storage economics, increased volatility is advantageous. Indeed, diurnal price spreads allow battery energy storage systems (BESS) to return their high capital costs by operating hundreds of cycles throughout the year. The combined occurrence of prolonged scarcity and surplus establishes a storage design requirement characterized by two opposing conditions: (1) prolonged high-price intervals requiring multi-day discharge capability, and (2) frequent low-price or curtailed-energy intervals enabling opportunistic charging. In both cases, the economic leverage increasingly shifts from incremental efficiency improvements to the ability to expand deliverable energy capacity at low marginal cost.

For electrochemical systems, energy capacity scales predominantly with cell mass and stack duplication, implying that extending discharge duration typically requires proportional investment in high-cost battery material. By contrast, geological storage media, such as solution-mined salt caverns, provide bulk storage capacity where the incremental energy capacity is dominated by subsurface volume, which can offer a materially lower marginal cost per additional stored MWh. This distinction becomes decisive when the required storage duration extends to multi-day or multi-week regimes, as suggested by the Dunkelflaute event class.

1.2 Acknowledgement of the need for long duration dispatchable power by policy makers

Over recent years, policy makers have identified the emerging need for long duration dispatchable flexibility. For example, Germany published that it would tender capacity for 10 GW of natural gas and long duration dispatchable power during 2026, Italy's first MACSE auction for energy storage resulted in 10 GWh of storage, at average durations of ~7 hours [5,6]. Over the years, the UK initiated several schemes to support low carbon dispatchable power through its Low Carbon Contracts Company (LCCC). More recently it issued the LDES cap and floor mechanism to promote grid-scale energy storage deployment for durations greater than 8 hours.

Electrification and adoption of LNG import reduced the demand for fossil fuel storage caverns substantially [7]. This resulted in overcapacity and the potential future abandonment of some storage caverns, unless repurposed. Existing pre-abandonment caverns may present a cost-effective and swift entry path for new technologies. However, it remains to be seen if demand for fossil fuel storage would change amid recent geopolitical developments in Iran.

1.3 Paper scope and structure

The present work translates the above LDES market drivers into a technical deployment framework for Airengy's CAPP concept based on isothermal CAES in solution-mined salt caverns. The paper

consolidates the technology status and recent engineering updates and formulates a subsurface-first site selection methodology emphasizing cavern eligibility, operating pressure window definition, and well/completion constraints that ultimately govern deliverable power and usable energy capacity. The Hilltop (UK) case study is used to demonstrate the practical application of this framework, integrating the Geostock conversion assessment to define the current candidate cavern set, the governing geo-mechanical and operational constraints, and the resulting basis of design. In addition, a dedicated technical treatment is provided for pipeline pressure losses under isothermal compressible flow, including the implications of tubing selection on energy losses and operating margins, and the debrining methodology for the HT04-HT06 system is described with an emphasis on operational sequencing and pressure-equalization requirements in potentially connected caverns. The work concludes by consolidating the key engineering constraints, execution considerations, and the near-term technical actions required to mature the project toward implementation.

2. Technology recap: Airengy's isothermal CAES and the CAPP architecture

2.1 AirBattery™ pillars

The CAPP is comprised of geological storage (solution mined salt caverns) powered by the AirBattery technology. The AirBattery system implements isothermal CAES using liquid piston technology. As opposed to conventional diabatic and adiabatic CAES utilizing air compressors and gas turbo-expanders, the AirBattery utilizes hydraulic pumps and turbines. The hydraulic equipment typically demonstrates higher energy conversion efficiencies and durability, especially under cyclic duty. The process is executed in modular pressure tanks (AirX™), through valve-controlled air and water paths, and hydraulic machines equipped with variable-frequency drives (VFD) to sustain high efficiency across a range of operating points.

Accordingly, the AirBattery concept is founded on three complementary technological pillars: (1) the patented AirX pressure tanks, (2) the liquid piston technology cycle as the core compression and expansion mechanism, and (3) a dedicated heat-exchange control architecture that actively governs air–water heat transfer to sustain near-isothermal operation across the full operating range.

2.1.1 AirX™ patented tanks

AirX pressure tanks are constructed on-site using construction-grade materials (steel rebar and cement) together with a proprietary polymer liner and are installed in a shallow buried configuration as illustrated in Fig. 2. The low-temperature character of near-isothermal compression enables polymer-based containment concepts, reducing reliance on massive bulk steel tanks and enabling burying the tanks, and minimizing system footprint (dual land-use). The AirX tanks received PED, CE, and ISO certifications (ISO 9001, ISO 45001, ISO 14001).

Figure 2. AirX™ tanks installed on-site at Nesher Israel Cement Enterprises Ltd (March 2022).

2.1.2 Liquid piston technology

The liquid piston cycle is realized by transferring water between two tanks through a reversible hydraulic machine, while air runs through valve-controlled connections to the atmosphere and the compressed air storage (CAS), as schematically illustrated in Fig.3 and Fig.4.

During CAS charging, water is pumped into an air-filled tank, thereby compressing the air while enabling rapid air–water heat transfer as shown in Fig. 3.

Once the tank pressure exceeds the CAS pressure, a valve opens and the remaining compressed air is displaced into the CAS, thereby incrementally raising the CAS pressure, consistent with the compression sequence presented in Fig. 3. Subsequently, the roles of the tanks alternate and the sequence is repeated until the CAS reaches its maximum operating pressure.

During CAS discharge, the sequence is reversed, with compressed air released from the CAS driving water displacement through the hydraulic machine to generate electrical energy, as illustrated in Fig. 4, and the cycle continues until the CAS reaches its minimum operating pressure.

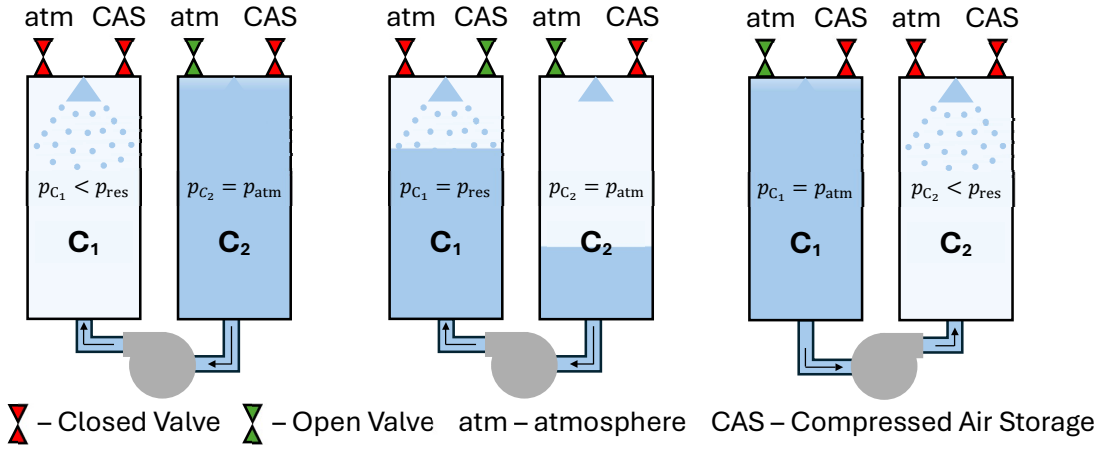

Figure 3. Fundamental concept of the Liquid Piston technology – Compression – Energy storage.

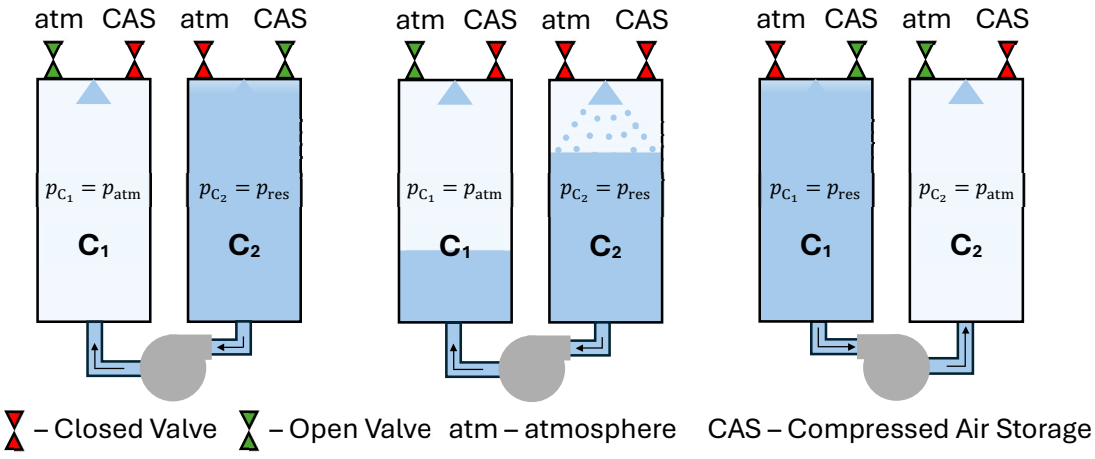

Figure 4. Fundamental concept of the Liquid Piston technology – Expansion – Energy release.

2.1.3 Heat exchange control architecture

Near-isothermal behavior is achieved through three coupled mechanisms: (1) a large air-water interfacial area and a stated thermal mass ratio exceeding 3500:1 (water-to-air) [8], (2) heat exchange to the surrounding ground due to underground installation and large surface area, and (3) a control architecture that actively sprays and circulates water via nozzle arrays to maximize mixing and convective heat transfer.

2.2 From AirBattery™ to CAPP

The isothermal nature of the AirBattery process negates any need for thermal compensation and doesn't require preheating of the expanding air using thermal storage and/or fossil fuels. Thus, when coupled with the AirBattery, the geological storage reservoir discharge duration is limited only by the energy in the reservoir. The scale of a cavern-connected CAPP is governed by three scaling dimensions:

1. Cavern volume. Multiple caverns can be considered at the same site for larger scale.
2. Cavern operating pressure window. This is constrained by mostly geo-mechanical aspects.
3. AirBattery power rating, which can be scaled through adding AirBattery modules, subject to well deliverability constraints.

This modular power plant concept is schematically illustrated in Fig. 5, showing the aggregation of multiple AirBattery modules into a CAPP utilizing multiple caverns.

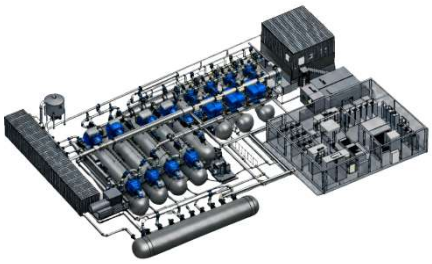

AirBattery™ Module

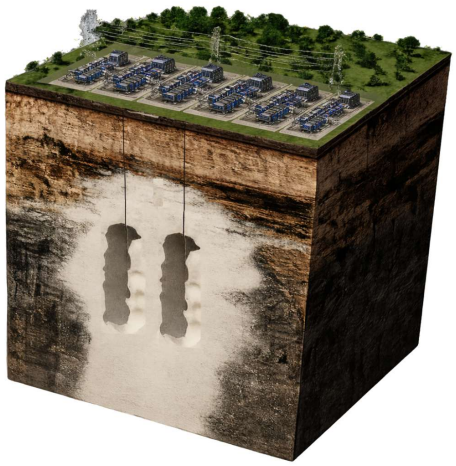

Compressed Air Power Plant (CAPP)

Figure 5. Modular power plant concept of the AirBattery™ technology into a cavern-connected Compressed Air Power Plant (CAPP)

3. Updates from last year (technical + commercial)

3.1 Cycle-time reduction

A key input to the AirBattery design and costs is the minimum time required to compress/expand air, while maintaining a near isothermal process. This input will be referred to as cycle time, and the goal is to reduce it as it would increase the power output from a given portion of air. During 2025, Airengy has conducted an extensive cycle-time test campaign at its demonstrator, to determine the minimum achievable cycle time. The experimental program followed two complementary optimization paths.

The first path focused on the spray heat-exchange subsystem. Here, multiple nozzle types were evaluated to optimize the trade-off between heat-transfer effectiveness from the fine water droplets to the air and the overall pump energy consumption throughout the cycle. In practice, atomization quality and droplet-scale interfacial area improve heat transfer, but they require additional pumping work to achieve the same flow rates. Accordingly, nozzle candidates were screened across multiple orifice sizes and spray angles to identify configurations that maximize air–water heat transfer per unit hydraulic power. Additional experiments regarding different layout arrangements for the nozzles are underway.

The second path tested the minimal cycle time required in the existing configuration that is installed in the demonstration plant in Yahel, Israel. To do so, multiple experiments were made in which an identical bubble of air was introduced to a water-filled tank. The expansion potential of the air bubble represented the energy input of the process. The bubble was allowed to expand at different cycle times, by opening the outlet toward the turbine. Larger outlet opening results in higher flows and faster expansion. Throughout the process the temperature of the air was monitored. A measurement of the volumetric flow (Q) and pressures (p) values at the water outlet, was used to calculate the process hydraulic energy output. By subtracting the energy output from the energy input, process losses were calculated. Cycle time was systematically reduced to identify the fastest operating regime that still preserves minimal losses, representing near-isothermal behavior. This demonstrated that the cycle time duration for the tested expansion ratio can be reduced by approximately 50% compared to prior testing. Further reduction may be achievable with further optimization of the nozzles' arrangement architecture.

The cycle time reduction leads to dramatic implications on scale and costs.

First, for a fixed machine rating, the same power output can be achieved by using smaller tanks and a faster compression and expansion process. Therefore, this enables a reduction in tank size while maintaining the same net power output.

Second, given tank volume can discharge faster, therefore delivering greater power output at the same cost and footprint. This enables the use of higher-rated hydraulic machines and increases plant power density without exceeding the geometric upper bound imposed by practical tank dimensions.

In summary, both paths result in an increase of the CAPP's power density in terms of MW/m^2, which provides a direct pathway to lower material quantities, reduced civil works, and overall CAPEX reduction.

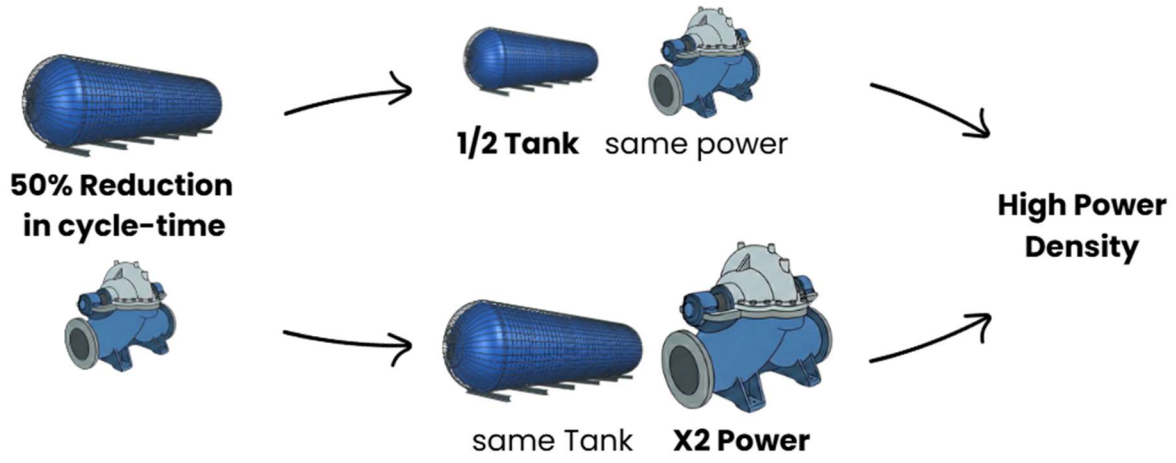

Figure 6. Impact of shorter cycle time on tank size and power density.

3.2 CAPP-BESS hybridization

During 2025, Airengy integrated an electrochemical battery energy storage system (BESS) into the AirBattery to improve the power profile. BESS integration allows the system to provide:

- black start capability
- Fast start-up and ramp-up times (participation in primary frequency reserve such as Ireland's DS3 services, which require responses as fast as 150 milliseconds, for example).
- Highly controllable power profile. Grid operators require generators to supply steady power output. AirBattery's power consumption and generation inherently oscillates. Highly responsive electrochemical batteries can balance these oscillations, maintaining constant power.
- Reduce required grid connection.

Lithium-ion batteries (procured from Tadiran New Energy) have been successfully integrated at the Yahel semi-commercial facility. Future AirBattery iterations may utilize supercapacitors due to their exceptionally high-power density, cyclability, and rapid transient response. The full control formulation for the hybrid system is provided in Appendix A. Fig. 7 illustrates this strategy.

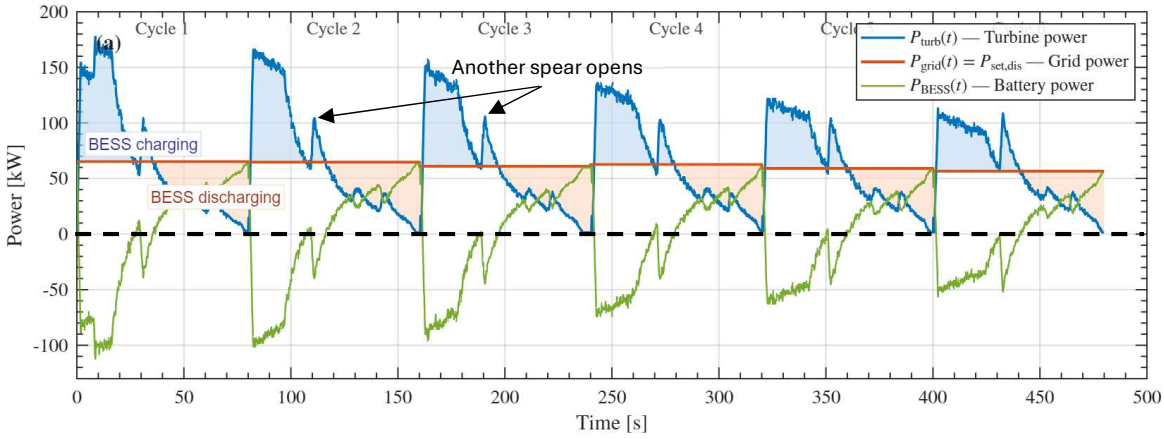

Figure 7. BESS hybridization across six consecutive AirBattery discharge cycles at the Yahel semi-commercial facility, with cavern pressure decreasing from 13.5 to 8.5 bar gauge (195.8 psig to 123.3 psig).

3.3 Automation Updates – Completely Remote and Autonomous Operation

In December 2025, the Yahel semi-commercial demonstration power plant was upgraded with a new system control architecture based on Siemens Totally Integrated Automation Portal (TIA Portal) program. The site is also monitored by live camera coverage throughout the system. This enhancement successfully transitioned the facility to 24/7, completely remote and autonomous operation availability.

4. Reusing former storage caverns for CAPP

4.1 Use of caverns for existing and under development CAES plants

The use of caverns for storage of compressed air has been successfully demonstrated at the Huntorf plant in Germany, commissioned in the 1970s, and the McIntosh plant in Alabama, USA, commissioned in the 1990s. In these installations, the caverns are located at depths of appx. 400–700 meters (1,300–2,300 ft), with operational pressures ranging from roughly 40 to 75 bar (roughly 600 to 1,100 psi). The subsurface parts of these installations reflect early design practices that do not fully align with current European subsurface storage industry standards, such as the double-well barrier principle. Both are so-called diabatic-CAES (D-CAES) installations, utilizing multistage air compressors to compress air into

high-pressure storage caverns, and a multi-stage turbo expander to harness the energy of the expanding air. To counter the extreme temperature fluctuations inherent in adiabatic compression and expansion and to maintain optimal operational temperatures throughout the process, the air is cooled after each compression stage and pre-heated before each expansion stage, by means of burning natural gas. Both plants do not incorporate heat storage.

In the past decades, several other CAES development projects have been started, both including D-CAES and adiabatic-CAES (A-CAES), like Corre Energy's hydrogen-fired CAES-projects in the Netherlands, Germany and Denmark [9], Gaelectric's Larne project (Northern Ireland) [10], the SANECA CAES project (Seneca Lake, Finger Lakes region, New York State) [11], and the A-CAES ADELE project in Staβfurt, Germany. None of these projects have yet materialized, and some have even been entirely terminated. One D-CAES project which is nearing start of construction, having secured all regulatory approvals, is Cache Power's 2 x 320 MW Marguerite Lake project in Northeast Alberta, Canada [12].

Also in China, in recent years, several new cavern projects have been commissioned, mostly as part of A-CAES installations, using above-ground heat storage tanks, like in Changzhou, Jiangsu Province (East China; 300 MWh; [13]), in Feicheng, Shandong province (1,800 MWh; [14]) and in Jiangsu (1,500 MWh; [15])

All these projects have in common that salt caverns are (or were supposed to be) used for storage of the compressed air, ranging in depth between appx. 400 meters (1,300 ft; Huntorf CAES plant) and appx. 1,300 meters (4,500 ft; Corre Energy's projects). This shows the wide depth range of caverns potentially suitable for CAES.

The information on the experiences with the actual use of caverns for CAES is relatively scarce and remains mainly limited to the well-studied Huntorf CAES-plant [16,17]. In general, it can be stated that, based on experience with other gases stored in salt caverns, caverns provide ideal, airtight locations for storing air under relatively high pressures (depending on depth). Nevertheless, using caverns and wells for storage of compressed air imposes several design challenges, including the effects of high-cyclic pressure changes on the tightness of the rock salt and the stability of the caverns, and the effects of the highly corrosive environment of humid air on the well completion [9]. These effects play an important role in selecting and designing caverns and wells for Airengy's AirBattery caverns as well and are further discussed below.

4.2 Specific aspects of salt caverns for Airengy's AirBattery

There are several aspects of salt caverns which play an important role when caverns are being used for storage of compressed air from the AirBattery, and which are to be considered when either selecting suitable caverns or designing and engineering caverns and wells to be transformed into compressed air energy storage caverns and wells.

4.2.1 General rock-mechanical and cavern stability aspects

The rock-mechanical and cavern stability aspects which play a role when designing storage caverns play an evenly important role when selecting or designing caverns for storage of air from the AirBattery. Fig. 8 presents the most critical design and operational parameters of storage caverns in graphical form [18].

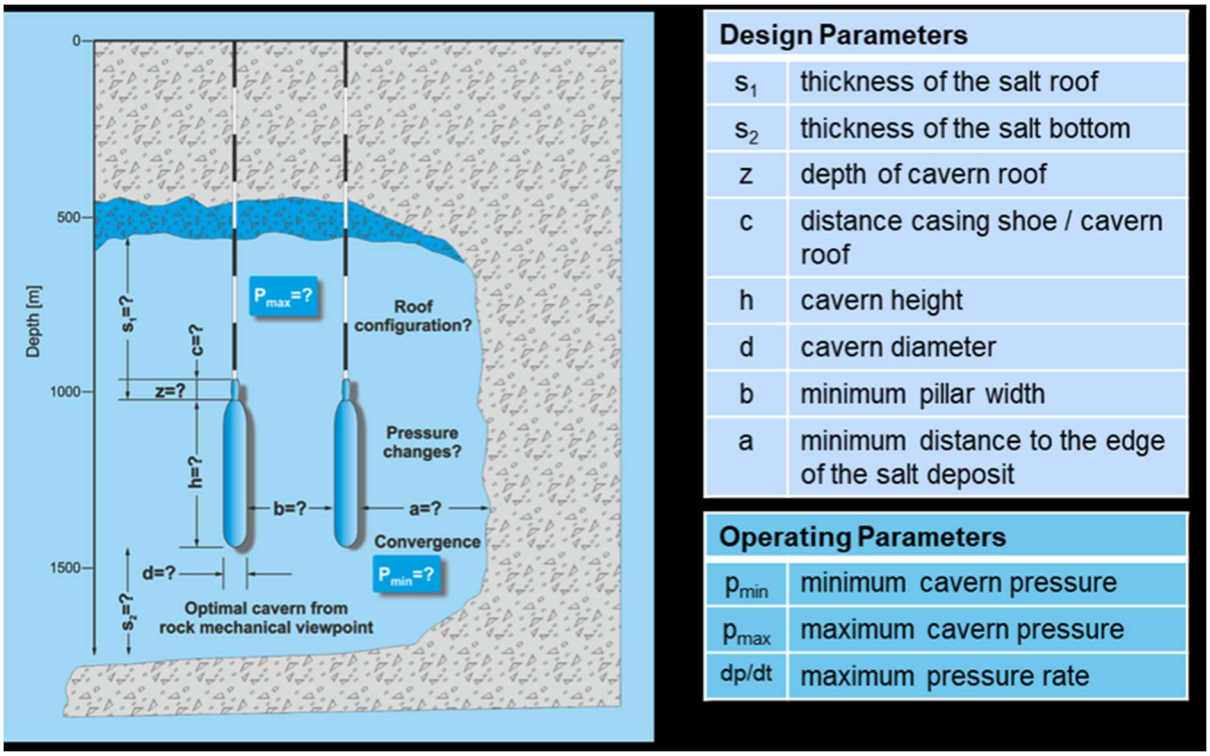

Figure 8. Important design and operating parameters of storage caverns in rock salt [18].

As with other storage purposes, the storage of compressed air in a specific salt cavern will require a dedicated, detailed rock-mechanical assessment to verify aspects like minimum and maximum pressures (to maximize the pressure range and therewith the cavern's energy capacity), acceptable pressure change rates, expected temperature fluctuations and other rock-mechanical consequences. This assessment should consider the relevant cavern specifications, the characteristics of air and the expected AirBattery operational requirements and expected storage patterns and will most probably result in several operational pressure ranges with different degrees of freedom, just as with natural gas and hydrogen storage [19].

4.2.2 Cavern depth and pressure

Salt caverns are found over a wide depth range, from several hundred meters (500 ft) to several kilometers (6,000 ft) of depth [20], resulting in a very wide range of related storage pressures, from appx. 20 bar (appx. 300 psi) in the shallowest caverns to over 300 bar (4,400 psi) in the deepest ones.

The maximum pressure that the cavern can hold is directly related to the cavern depth (i.e., the distance between the earth's surface and the top of the cavern), and the maximum pressure is typically determined by the strength of the Last Cemented Casing Shoe (LCCS) of the well, being the deepest point of the most deeply cemented casing in contact with the surrounding rock. In general, the maximum allowable storage pressure is set as a fixed percentage of the lithostatic pressure, for example 80%.

Airengy's AirBattery is highly flexible in the pressure range it can handle. By simply adding compression and expansion stages and employing turbomachinery tailored for each stage, higher pressures can be reached during the compression cycle and highly pressurized air can be used for electricity generation during the production cycle [8]. In this way, higher storage pressures simply lead to a larger energy production (higher power range). In the meantime, the higher storage pressure means that a larger mass of air is being stored, increasing the amount of stored energy. So, the cavern and LCCS depths, together with the cavern volume of course, are the most important factors determining the potential energy which a salt cavern can hold when utilized for storage of compressed air. In this way, it differs from storage of natural gas or hydrogen, where a high (working gas) mass is the most important reason for pursuing a large storage pressure.

Next to the maximum pressure, also the minimum pressure is an important aspect as these two together determine the storage pressure range. A larger range leads to a higher potential storage energy content of the cavern, while a smaller range gives a smaller content. Commonly, the minimum pressure is set as a percentage of the lithostatic pressure or as a percentage of the maximum pressure. But in some specific cases, a different value is used due to local rock-mechanical circumstances.

4.2.3 Cavern volume and usable storage volume

Salt caverns come in many sizes, ranging from several tens of thousands of cubic meters (several 100,000 bbl) to over 4 million cubic meters (over 25 MMbbl). Together with the pressure, the cavern volume is directly proportional to the compressed air energy storage potential. An aspect to consider is that potential energy must be transported to the surface via the storage well. As most caverns only have one well, the well size limits the maximum mass flow and therewith the maximum power output of the connected AirBattery. Therefore, larger caverns quickly result in a longer duration of electricity production, rather than in an increased power output.

In some situations, the usable storage volume differs from the cavern volume. The three main reasons are:

1. An uneven cavern floor may not allow for complete debrining of the cavern, for example in case the debrining string cannot reach the deepest point of the cavern.
2. Cavern wall overhangs or so-called ‘salt fingers’ pointing into the cavern may not allow for debrining of the cavern below a certain depth level.
3. A shallow LCCS depth with respect to the desired debrining depth level may limit the maximum pressure during debrining and therewith the maximum debrining depth.

4.2.4 Storage capacity

Together, the maximum pressure, the storage pressure range, and the usable cavern volume determine the cavern energy storage capacity when used for compressed air energy storage. In combination with the energy production efficiency of the AirBattery of 80%, for each cavern, the AirBattery capacity (in MWh) can be determined. If this capacity indeed can be used depends, among other things, on the availability of enough well-capacity for transportation of the compressed air to surface. In this way, the power capacity of a single AirBattery plant with a quite common cavern volume of 350,000 m^3 (2.2 mln bbl) at a depth of appx. 550 meters (1,800 ft) can already deliver 1.6 GWh of energy, which is more than the Huntorf plant's capacity of appx. 1 GWh, which even requires burning a significant amount of natural gas to deliver that capacity.

4.2.5 Storage wells and well completion

Just as caverns, the cavern wells come in multiple shapes and sizes too. Most deeper caverns (>500 meters; > 1,600 ft) and most (former) storage caverns have Last Cemented Casings (LCCs) between 9-5/8” and 13-3/8”, which can hold a 7” up to a 9-5/8” production tubing. But known CAES caverns, like Huntorf and McIntosh, have much larger wells, Huntorf for example has a 24-1/2" LCC, holding a production tubing of some 20-21” [16]. Furthermore, nearly all caverns are equipped with one single well; the number of caverns with multiple wells is relatively small.

As Airengy is focusing on using existing caverns for their AirBattery, the maximum flow velocity (and therewith the maximum mass flow of compressed air) is an important limiting factor determining the power output of the AirBattery plant. Fortunately, this power output is rather flexible as well, ranging from less than one to multiple MW, and Airengy is focusing on long duration storage (multiple days up to multiple weeks), rather than on short duration storage as are most of the existing CAES plants (with production durations of several hours up to one day). The long duration focus strongly reduces the required air flow. Still, maximizing the production tubing diameter is an important aspect, as it helps reduce pressure losses due to friction over the full length of the well. In some cases, drilling a second well into an existing cavern might be an even better solution.

A second important aspect regarding the storage wells is the highly corrosive character of humid compressed air. When reusing existing storage caverns, in general, the present completion is assumed to be not suitable for air storage, or at least not for a very long time, as the high corrosive circumstances caused by the air in a salty environment require highly corrosion-resistant materials for each piece of equipment in direct contact with the air.

If a new completion is to be installed, its parts that are in contact with compressed air should be designed for dedicated compressed air storage operation. In general, for CAES, three well completion options are assumed feasible (see Fig. 9):

a. A gas storage-like production tubing + packer completion (i.e. a monitorable double barrier design), all made of highly corrosion resistant material
b. A highly corrosion resistant, free-hanging production tubing completion with a slightly over-pressurized, nitrogen-filled annular space like in Huntorf (Germany) and McIntosh (US) (i.e. a semi-monitorable semi-double barrier design)
c. A cemented highly corrosion resistant liner completion (unmonitorable double barrier design).

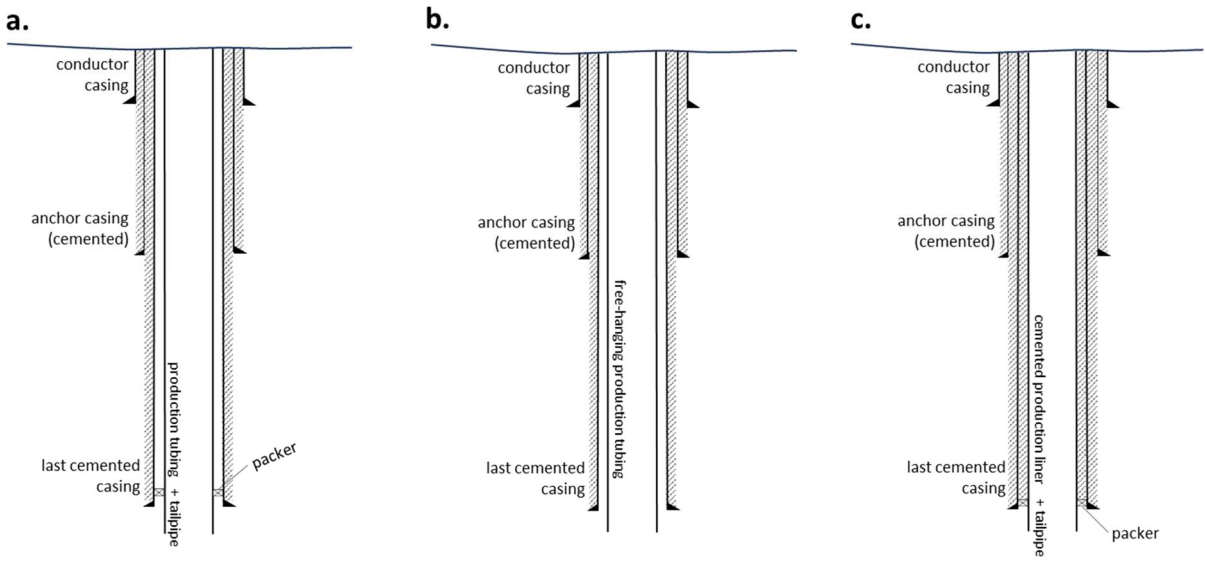

Figure 9. Possible well completion options for the AirBattery.

For the moment, the first option, being in line with present gas storage completions, is assumed to be the most feasible, but the two alternative options are looked at as well. Determining the most suitable well completion both from an energy and from a corrosion resistivity point of view is the main subject of the ongoing well engineering phase for the potential AirBattery caverns. The local and cavern specific situation might demand other well completion options.

Further to the use of corrosion resistant materials, drying the air before it enters the cavern is an important preventive measure as well. In regular CAES facilities, this is part of the compression cycle. In the intercoolers, which are placed between the multiple compression steps, most water is removed. As there are no intercoolers present in the AirBattery (as these are not necessary due to the isothermal character of the system), an extra dehumidification step is required to remove most of the water from the air before it enters the cavern. Otherwise, extra water would be added to the cavern during each injection phase, which might cause further undesired leaching of the cavern, and may lead to extra corrosion of the well completion.

It is difficult to predict whether the outgoing air will contain a lot of water. Temperature changes in the cavern are expected to be relatively small, only fluctuating appx. 5°C (9°F) up and down during compression and expansion respectively, and the rock salt has a drying effect on the air in the cavern. Preliminary calculations show a relative humidity of 93%. Together with the fact that the outflowing air may contain salt dust, the use of highly corrosion resistant materials for the well completion is highly required.

4.2.6 Other aspects of reusing existing caverns

Next to the aspects described above, there are several other aspects which play a role when caverns, which have previously been used for storage of other substances, are going to be deployed for compressed air storage. The most important one is the possibility of former storage products which may have intruded into the salt or may remain present in pockets on the roof of the cavern or on the walls under localized overhangs. Especially in the case of stored hydrocarbons, this may be an issue, as the air returning from the cavern is not burnt in the AirBattery (as in a D-CAES plant), but is being vented to the atmosphere. Furthermore, most hydrocarbon storage permits include the obligation to retain as much as possible storage substances once the storage is terminated.

To reduce odor issues and to limit explosion risks, it is deemed necessary to take all possible measures to remove any remaining volumes of hydrocarbons from the cavern. The most logical way to do this is by making a detailed sonar measurement of the roof and wall, followed by a dedicated cavern re-leaching phase, during which both roof pockets are being minimized, overhangs are removed and the possibly hydrocarbon containing skin of the cavern is leached away.

4.3 Cavern options in NW-Europe

During the past year, Airengy has been in touch with many cavern developers and operators regarding the potential use of salt caverns for being deployed for compressed air storage, either in a small-scale demonstration project or in a commercial size CAES project. The most promising options are in Germany, with its abundant number of caverns at different locations, depths and volumes, and in the UK, which holds appx. 400 caverns, of which appx. 150 are being used for storage of a large diversity of products, including natural gas in over 100 caverns. These caverns are mainly at relatively shallow depths (250-700 meters (800-2,300 ft)) and have relatively small volumes (appx. 300,000 m^3 (1.9 MMbbl) on average, ranging from as little as 10,000 m_3 (63,000 bbl) to over 600,000 m^3 (3.8 MMbbl)) [20]. But also in less obvious countries, like Romania, there is potential to develop small-scale AirBattery sites.

4.4 Site Selection Methodology for CAPP

Infrastructure investments are capital intensive and for scaled up commercial deployment to be viable, institutional financing is required. Despite the progress of the AirBattery technology over recent years, the technology is still not bankable. Airengy is pursuing a larger scale cavern connected facility to be funded by its equity investors, with a goal of reaching commercial technology readiness level that is bankable (TRL 8). The UK LDES Cap and Floor Mechanism provides an example of the importance of this milestone. Developers of novel technologies featuring an operating facility with a discharge power greater than 1MW, can utilize the mechanism to qualify for government support. The support is provided through debt guarantee and is subject to proposed facilities with a discharge power greater than 50MW. During 2025, Airengy had been in discussions with multiple potential sites for the first cavern connected facility, with a focus on the European market. After a thorough vetting process, the Kistos Energy Storage site was selected. The site was acquired by Kistos from EDF in 2024 along with its key personnel.

4.4.1 Geological context

The Hilltop and Hole House cavity field is located within the Cheshire Basin, a broad Triassic sedimentary graben filled with thick sequences of evaporites and mudstones. The cavities were developed within the Northwich Halite Formation, 200 meters (656 ft) thick middle-Triassic rock-salt unit

belonging to the Mercia Mudstone Group. The Northwich Halite is made of alternating beds of relatively pure red-brown rock salt interlayered with thin mudstone bands. Across the site, the depth to the halite varies from 180 to 230 meters (590–755 ft), with an overall stratigraphy dipping southeast at about 3%. The overlying formation consists of 18 meters (59 ft) of Quaternary drift deposits and a thick (~190 meters, ~623 ft) sequence of Middle Mercia Mudstone, composed of red and green-grey mudstones and siltstones with occasional anhydrite nodules. Below the halite, the sequence transitions into the Lower Mercia Mudstone. Structurally, the site lies in the hanging wall of the Cheshire Graben system, in proximity to the regional King Street Fault (located approximately 200 meters (656 ft) to the east of the site).

4.4.2 Cavity field

Since 1975, Tata Chemicals (formerly British Salt) has operated the Warmingham Brinefield on the Hilltop (Fig.10) and Hole House Farm sites. Since work commenced, more than twelve completed cavities have been created, and others are being developed to the east of the existing cavities (approximately 200 meters (656 ft) away from the existing wells).

Between 2001 and 2009, four Hole House cavities were converted for gas storage and operate between 20 and 55 bar gauge (290 and 797.7 psig) (with a cavity volume between 230,000 and 340,000 m³ (1.45 and 2.14 MMbbl)). Five Hilltop cavities (HT07, HT09, HT10, HT11, and HT12) were converted between 2010 and 2018 and operate between 29 and 45 bar gauge (420.6 and 652.7 psig) (cavity volume between 610,000 and 670,000 m³ (3.84 and 4.21 MMbbl)). The remaining cavities are kept filled with brine and maintained at constant pressure.

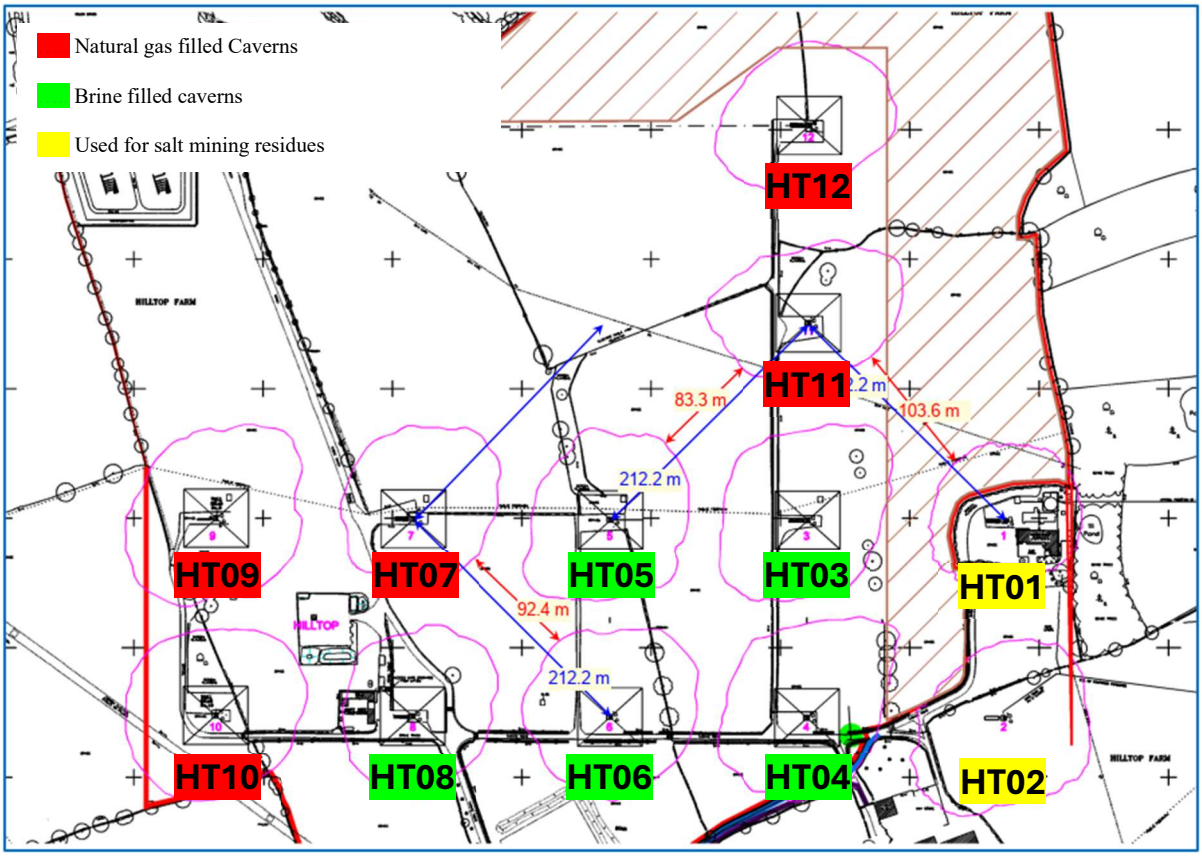

Figure 10. Hilltop cavern field map (north direction is horizontal to the right)

Amongst the considerations for selecting the site are:

1. Planning consent timeline: Under EDF's ownership, the Kistos Energy Storage site team demonstrated its capabilities to secure local planning consent for an adiabatic compressed air energy storage project, proposed by Hydrostor.
2. Module sizing: While at higher pressures the AirBattery cost per kW is lower (due to smaller flows, resulting in smaller machinery and piping), a high-pressure module would result in high power requirement. The Kistos site is characterized by a relatively shallow salt layer, resulting in low operating pressures. This allows for a relatively small module design and lower project capex.
3. Scalability: Over the coming decade Kistos expects that the gas storage activity will concentrate on the Hole House cavern field, and that the Hilltop caverns will become available for CAPP implementation. In addition, the Hole House field has potential for additional caverns. The proximity of the site to the British Salt processing plant, provides potential for additional caverns to be mined economically, as British Salt may serve as an offtaker for the salt. This would allow a grid-scale CAPP supported by the UK LDES cap and floor mechanism.
4. Market readiness- The UK is renowned as a global leader in energy transition. It demonstrated its commitment to low carbon dispatchable power through different technologies. Aside from the LDES cap and floor mechanism, it has implemented mechanisms for grid scale nuclear and bio-mass generators. In addition, the Kistos site is located within the heart of England where there is strong demand for electricity.

4.5 Cavern Selection Considerations at Hilltop Site

This section provides a preliminary geo-mechanical assessment of converting brine-filled Hilltop caverns into CAES facilities. It identifies the most suitable caverns for conversion and recommends operating parameters.

4.5.1 Rationale for Selecting the HT04-HT06 Caverns

For compressed air storage, a spherical cavern shape is optimal from a rock-mechanical perspective, while tall cigar-shaped caverns make the most efficient use of the underground volume. As a practical compromise, oval to bottle-shaped caverns with a height-to-diameter ratio of 2 to 3 are considered ideal. Such caverns should be supported by wide salt pillars and located away from natural-gas storage caverns (to avoid cross-cavern pressure differentials and the risk of air or gas migration).

The standard spacing design between gas caverns usually incorporates a pillar-to-diameter ratio between 1.5 and 3, depending on the mid-depth of the cavern. In the Hilltop field, however, the minimum salt pillar thickness between caverns is only about 16 meters (52 ft), while cavern diameter reaches up to 130 meters (427 ft), deviating from standard practice. The conversion of the cavities was carried out gradually using restricted operating parameters ("soft cycling") and is continuously monitored by a microseismic array. Sonar measurements show that the cavities have remained stable since they were operated in gas between 2010 and 2018, and no communication between the cavities has been detected during operations.

Cavern HT05 was identified as a possible candidate for conversion once HT07 would cease to store natural gas. However, the distance from natural gas-filled HT11 is only about 80 meters (262 ft) and therefore it is considered less suitable for CAES in a preliminary study by Geostock. Among the brine filled caverns, HT04 and HT06 are considered the most favorable as they are located further away from the natural gas storage caverns and are positioned behind "screen" cavities. An interesting feature regarding HT04 and HT06 caverns, is that they are hydraulically connected, and specific attention must be given to the possible impact of this connection on their operating conditions and stability.

The conversion of HT04 and HT06 for natural gas storage was not recommended due to the uncertainties regarding roof stability as evidenced by past numerical modeling studies. Geostock's preliminary rock-mechanical study shows that when operated within strict pressure constraints, pool operation of these two caverns for compressed air storage is feasible.

Hilltop natural gas caverns currently operate between 29 and 45 bar gauge (420.6 and 652.7 psig), with pressure change rates limited to 4 bar/day (58 psi/day) in the 35-45 bar gauge (507.6-652.7 psig) range and 2 bar/day (29 psi/day) in the 29-35 bar gauge (420.6-507.6 psig) range. Originally, stricter limits were recommended, which were later eased following additional numerical modeling and soft cycling tests.

As a preliminary approach and in the absence of detailed modeling, for CAES operation the following initial operating parameters are considered acceptable from a geo-mechanical perspective.

4.5.2 Minimum Operating Pressure

The minimum operating pressure in the HT04 and HT06 cavern system is estimated at 31 bar gauge (450 psig), corresponding to the saturated brine pressure at the lower level of the HT06 cavern roof at 260 meters (853 ft) depth. At this pressure, the estimated vertical stress in the salt pillars yields a dilation safety factor of 2, and the salt thickness above the caverns meets the minimum requirement derived from classical plate theory for roof stability. However, fatigue behavior of the rock and long-term degradation of the claystone layers have not been accounted for. The supporting calculations and the simplified cavern layout used for the pillar stress assessment are provided in Appendix B.

4.5.3 Maximum Operating Pressure

The maximum cavern pressure is set to prevent the infiltration of gas or air into the surrounding rock mass and adjacent caverns, defined as the pressure at which the effective tangential stress at the cavern roof becomes tensile. Applying the gas infiltration criterion with a far-field lithostatic stress gradient of 0.022 MPa/m and a brine pressure gradient of 0.012 MPa/m, the maximum air pressure at the HT04 cavern roof (245 meters depth – 804 ft) is 37.5 bar gauge (544 psig). The derivation is provided in Appendix B.

4.5.4 Guarantee of maintaining minimum pressure

A critical operational constraint is that the caverns must never be depressurized below the recommended minimum operating pressure ($p_{\mathrm{min,cavern}}$), as this would risk severe and irreversible damage to cavern roofs and pillars, potentially causing localised collapse or sinkholes. For the gas storage caverns this is achieved by having surface-controlled subsurface safety valves (SCSSSVs) installed in the gas storage wells.

5. Basis of Design (BoD) for Hilltop CAPP

5.1 Wells and Caverns Data

Table 1 summarizes the main parameters of the wells considered for CAES conversion. These data comes from various sources and may be inaccurate.

Table 1. Hilltop HT04 & HT06 wells data.

Hilltop data	**Unit**	**HT04B**	**HT06B**
Glacial till	m bgl	0	0
Sidmouth Mudstone	m bgl	20	20
Northwich Halite	m bgl	205	211
Cavern roof	m bgl	246	252
Cavern bottom	m bgl	326	334
13 3/8 shoe	m bgl	225	221
Volume	m^3	692,840	628,957
Max radius	m	95	82
Cavern height	m	80	82

The HT04 and HT06 caverns are assumed to be hydraulically connected as can be seen in Fig. 11, and sonar measurements suggest a connection at a depth of approximately 288–296 meters (945–971 ft), although the connection geometry and size require confirmation by detailed sonar. If the connection exists and is large enough – order of 2 meters (6.6 ft) diameter – it can materially change how the two caverns behave during air storage.

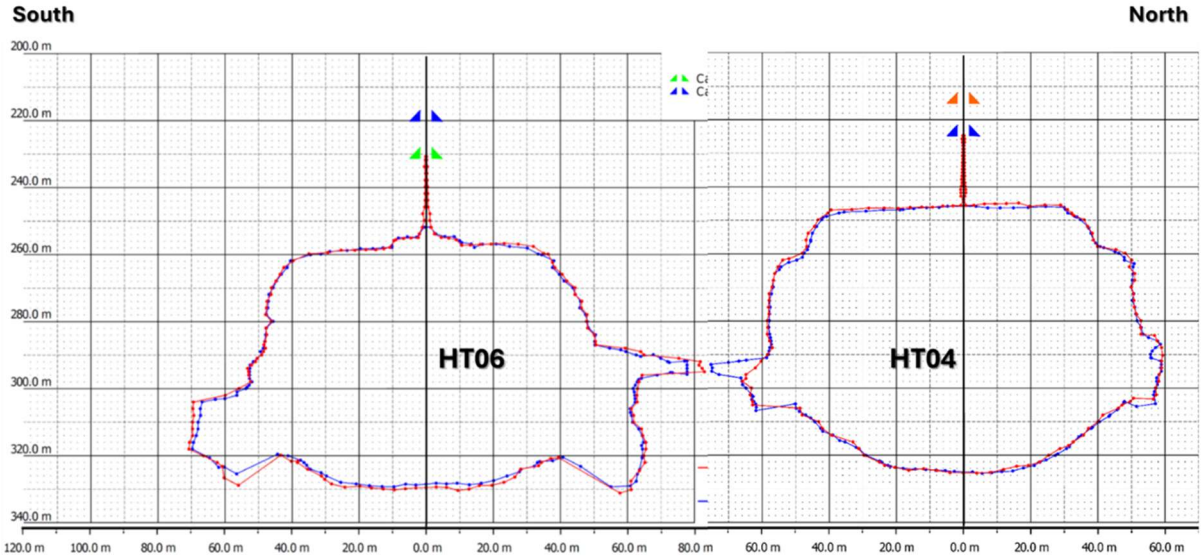

Figure 11. Cross section through caverns HT06 (left window) and HT04 (right window), possibly connected.

Two operating states are identified, governed by the position of the brine–air interface relative to the connection:

1. **Pneumatic connection (air–air connection):** the two caverns effectively act as one larger air-filled cavern, with air flowing through the connection to equalize pressure differences. Achieving this requires air-filling both caverns down to at least the bottom of the connection, corresponding to a total air storage volume of approximately 713,000 m^3 (4.48 MMbbl) – HT06 ~261,000 m^3 (1.64 MMbbl) and HT04 ~452,000 m^3 (2.84 MMbbl).

2. **Hydraulic connection (brine-filled connection):** the connection remains in brine, and the two caverns do not behave as a single air space. In this case, geometry differences matter because HT04 is positioned approximately 13 meters (42.7 ft) shallower than HT06, and near the connection level the storage volume of HT04 which is ~394,000 m^3 (2.48 MMbbl) is almost twice that of HT06 which is ~216,000 m^3 (1.36 MMbbl). Under equally distributed injection or withdrawal, HT06 will experience larger pressure changes than HT04, leading to a small brine-level difference between the two caverns.

In the hydraulic connection operating stage, the liquid piston technology operating behavior as described in paragraph 2.1.2 and the cycle time (see paragraph 3.1) allow for a natural equalization mechanism. Air portions are transferred to or from the cavern during about 60% of the cycle time, followed by 40% with no flow, allowing the system to equalize within every cycle. During this equalization, a relatively small brine volume which is roughly 20 m^3 (706 ft^3) is expected to flow through the connection from HT04 to HT06, and if the connection is sufficiently large, this horizontal brine displacement is not expected to negatively impact stability, subject to validation by sonar and detailed rock-mechanical assessment.

In the present project framing, the preferred operating concept is to debrine and operate below the connection. The main reason for that is to maximize the usable air volume of the cavern and therefore maximize the deliverable storage energy in terms of kWh.

5.2 Well completion status

The HT04 and HT06 wells have been relined in 2014 with a 10-3/4" x 9-5/8" cemented casing and completed in 2016 with a 7" tubing-packer completion and a new wellhead. No SSSV is currently installed in the wells.

The wells have been retested in 2016 prior to the installation of the 7" tubing with nitrogen tests that showed no leaks in the wells at the maximum operating pressure. During these tests, no hydraulic connectivity was observed between the HT04-HT06 system, and any of its neighbors.

Based on preliminary results from the Atkins well completion study, re-use of the existing 7" completion appears feasible for the first-of-a-kind (FOAK) project, subject to confirmation of a proposed alternative shut-off solution and a corrosion assessment for wet-air service over the expected FOAK duration. However, the existing completion is not expected to be suitable for continued use beyond the FOAK phase. Replacement of the well completion is therefore anticipated for any subsequent long-duration or full-scale development.

5.3 Maximum Isothermal Work Extraction from a Cavern

Consider a cavern of fixed geometric volume V_{cavern} filled with ideal air at constant temperature T. During discharge, air flows from the cavern through the well to the surface, arriving at the wellhead at a pressure that differs from the cavern pressure due to the hydrostatic column and frictional losses in the well (as characterized in Appendix C). The AirBattery surface equipment operates against the wellhead pressure, so the extractable work is governed by the wellhead pressure swing rather than the cavern pressure swing.

The maximum theoretical work extractable over the wellhead pressure swing can be expressed as the difference between the isothermal expansion work against the atmosphere evaluated at the two wellhead operating limits:

$$W_{\text{max,cavern}} = W_{p_{\text{max,wh}} \to p_0} - W_{p_{\text{min,wh}} \to p_0} \qquad \text{(Eq. 1)}$$

For air leaving the cavern at a given wellhead pressure p_{j} (where $p_{\text{min,wh}} \le p_{\text{j}} \le p_{\text{max,wh}}$), the isothermal expansion work against atmospheric pressure p_0 is

$$W_{(p_{\text{j}} \to p_0)} = p_{\text{j}} V_{\text{cavern}} \ln\left(\frac{p_{\text{j}}}{p_0}\right) - V_{\text{cavern}}\left(p_{\text{j}} - p_0\right) \qquad \text{(Eq. 2)}$$

Substituting Eq. (2) into Eq. (1) yields the maximum work extractable over a full discharge cycle:

$$W_{\text{max,cavern}} = V_{\text{cavern}} \cdot \left[p_{\text{max,wh}} \ln\left(\frac{p_{\text{max,wh}}}{p_0}\right) - p_{\text{min,wh}} \ln\left(\frac{p_{\text{min,wh}}}{p_0}\right) - \left(p_{\text{max,wh}} - p_{\text{min,wh}}\right)\right] \qquad \text{(Eq. 3)}$$

Eq. (3) is the thermodynamic upper bound for an isothermal, lossless surface process. Real work will be lower due to turbines, VFD, motor, and process efficiencies. The wellhead pressures $p_{\text{max,wh}}$ and $p_{\text{min,wh}}$ correspond to the cavern operating pressures $p_{\text{max,cavern}}$ and $p_{\text{min,cavern}}$ adjusted for the well pressure profile derived in Appendix C.

5.4 Design Rating and Storage Objective

Because cavern pressure changes are limited to a few bars per day and the storage is underground with negligible temperature variations over the cycle, the maximum extractable energy is conveniently estimated using an isothermal available work upper bound. This approach is also consistent with the near-isothermal design intent of the AirBattery conversion process.

The combined geometric volume of the selected caverns is taken from the well data as 692,840 m^3 (4.36 MMbbl) for HT04 cavern and 628,957 m^3 (3.96 MMbbl) for HT06 cavern, therefore the total volume of the HT04–HT06 doublet system is 1,321,797 m^3 (8.31 MMbbl). With the recommended CAES pressure window of 31–37.5 bar gauge (450–544.0 psig), the corresponding absolute pressures are 32.0–38.5 bar absolute (464.1–558.4 psia).

Using Eq. (3) with p_0 = 1.01325 bar absolute (14.696 psia), the theoretical maximum available energy for the full HT04–HT06 geometric volume is:

For the 31–37.5 bar gauge (32–38.5 bar absolute) case: $W_{\max}$ = 846.8 MWh (2,890 MMBtu)

If future geo-mechanical studies and operational experience would allow the operating window to be widened to the existing gas-storage range of 29–45 bar gauge (30–46 bar absolute), and if the full volume can be used, the maximum available energy would increase to: $W_{\max}$ = 2,125 MWh (7,250 MMBtu)

From a CAPP system perspective, a key benefit is that the design can accommodate the power and duration requirements by combining AirBattery surface modules, while duration and total stored energy can be scaled primarily through cavern volume and the selected operating pressure window, enabling flexible matching of plant rating and storage objective to the target market.

6. Pressure Losses in Wells and Pipelines

6.1 Analytical Model for Isothermal Compressible Flow in Inclined Pipelines

This section presents an analytical model for the pressure distribution along an inclined pipeline under steady-state air flow. The model assumes isothermal conditions, compressible ideal-gas behavior, constant internal diameter, and combined wall-friction and fitting losses modeled using the Darcy-Weisbach formulation. The objective is to calculate the outlet pressure p_{out}as a function of the inlet pressure p_{in}across a pipeline segment of length L, accounting for friction, localized losses, and gravitational static head. The flow-direction angle convention is defined in Fig. 16 in Appendix C ($\theta = 90°$ for vertical upward flow, $\theta = 270°$or $-90°$for vertical downward flow).

The full derivation is provided in Appendix C. Two coefficients are introduced to consolidate the physical parameters: coefficient $a$captures the mechanical energy losses from wall friction and fittings, and coefficient $b$captures the hydrostatic forces governed by gravity, temperature, and pipeline inclination (defined in Appendix C, Eqs. C.19 and C.20).

The total pressure change across the inclined segment is:

$$\Delta p_{\text{total}} = p_{\text{out}} - p_{\text{in}} = \sqrt{\left(\frac{a}{b} + p_{\text{in}}^2\right) e^{2bL} - \frac{a}{b}} - p_{\text{in}} \qquad \text{(Eq. 4)}$$

This total pressure change can be decomposed into two independent components. The frictional and localized loss component, evaluated for horizontal flow where gravitational effects are negligible ($b = 0$), is:

$$\Delta p_{\text{loss}} = p_{\text{out,loss}} - p_{\text{in}} = \sqrt{p_{\text{in}}^2 + 2La} - p_{\text{in}} \qquad \text{(Eq. 5)}$$

The hydrostatic elevation component, evaluated for frictionless flow ($a = 0$), is:

$$\Delta p_{\text{gravity}} = p_{2_{\text{gravity}}} - p_{\text{in}} = p_{\text{in}} e^{bL} - p_{\text{in}} = p_{\text{in}}(e^{bL} - 1) \qquad \text{(Eq. 6)}$$

6.2 Well Pressure-Loss Characterization and Operating Flow-Rate Envelope

The analytical model derived in Section 6.1 is applied here to characterize the pressure losses in the HT04 and HT06 wells under the anticipated CAES operating conditions, and to evaluate tubing size selection for single-well and dual-well configurations.

6.2.1 Well geometry and tubing candidates

Table 2 summarizes the candidate tubing sizes considered for the well completion, following the Geostock conversion assessment [21]. The 5-1/2" options use heavy-wall pipes to provide margin against long-term corrosion in wet-air service, while the 7" tubing is based on the dimensions of the pipe currently installed in the well. The pipe lengths are defined by the vertical distance from the surface to the cavern roof, which is 246 meters (807 ft) for HT04 and 252 meters (827 ft) for HT06.

Table 2. Candidate tubing sizes considered for the well completion

Tubing Size	OD [mm]	ID [mm]	Wall thickness [mm]
5-1/2"	139.7	108.0	15.9
7"	177.8	157.1	10.4

6.2.2 Flow-rate operating envelope

The mass flow rate during the dynamic phase of each AirBattery cycle is governed by the cavern pressure and the cycle timing. Consider a case of a 1.6 MW Airbattery module utilizing a total shared volume of 650,000 m^3 (4.09 MMbbl) of the HT04-HT06 system. At the minimum cavern operating pressure which is 31 bar gauge (450 psig) for the investigated case, the total mass flow rate is approximately 10.9 kg/sec (24 lb/sec), while at the maximum operating pressure which is 37.5 bar gauge (544 psig) it increases to approximately 13.9 kg/sec (30.6 lb/sec). At lower cavern pressures, the pressure of the cavern equalizes with the tank pressure earlier in the cycle, resulting in a longer flow phase within the fixed cycle period.

For dual-well operation, where HT04 and HT06 operate in parallel, the total flow is split approximately equally between the two wells, yielding per-well flow rates of about 5.45–6.95 kg/sec (12–15.3 lb/sec).

The conversion between mass flow rate and standard volumetric flow rate is given by:

$$Q_0 \left[\frac{\mathrm{Nm}^3}{\mathrm{day}}\right] = \dot{m}_{\mathrm{air}} \cdot \frac{R_{\mathrm{air}} T_0}{p_0} \cdot 86{,}400 \qquad \text{(Eq. 7)}$$

where T_0 and p_0 define as the temperature and pressure respectively at normal conditions. At the average operating flow rate of approximately 12.4 kg/sec (27.3 lb/sec), this corresponds to roughly 828,900 Nm^3/day (29.27 MMscfd).

6.2.3 Distinction between pressure loss and energy loss

Pressure loss and energy loss are related but not identical quantities and should not be interpreted interchangeably. The percentage pressure loss between the cavern roof and the wellhead is

$$\Delta p_{\mathrm{loss}}[\%] = 100 \cdot \frac{p_{\mathrm{wh,ideal}} - p_{\mathrm{wh,act}}}{p_{\mathrm{wh,ideal}}} \qquad \text{(Eq. 8)}$$

where $p_{\mathrm{wh,ideal}}$ is the wellhead pressure at zero flow (gravity-only static head) and $p_{\mathrm{wh,act}}$ is the actual wellhead pressure under flow conditions. By contrast, the percentage loss in available useful work, derived in Appendix E for a single AirBattery discharge cycle expanding to atmospheric pressure, is

$$E_{\mathrm{loss}}[\%] = 100 \cdot \frac{\ln\left(p_{\mathrm{wh,ideal}}/p_{\mathrm{wh,act}}\right)}{\ln\left(p_{\mathrm{wh,ideal}}/p_0\right)} \qquad \text{(Eq. 9)}$$

Therefore, energy losses are substantially smaller than pressure losses.

6.2.4 Wellhead pressure curves

Figs. 12 and 13 present the wellhead pressure and the corresponding loss percentages as a function of total mass flow rate for the two candidate tubing sizes – 5-1/2" (ID 108.0 mm / 4.252 in) and 7" (ID 157.1 mm / 6.185 in) – computed using Eq. (4) with the following parameters: $\bar{f}$ = 0.0165, T = 293.15 K (20 °C / 68 °F), K_{Σ} = 0, and θ = 90° (vertical upward flow during discharge). Each tubing size is plotted at both the minimum cavern operating pressure of 32 bara (31 bar gauge / 464 psia) and the maximum of 38.5 bara (37.5 bar gauge / 558.4 psia). Vertical markers indicate the expected operating flow rates at $p_{\min}$ (10.9 kg/s / 24.0 lb/s), average (12.4 kg/s / 27.3 lb/s), and $p_{\max}$ (13.9 kg/s / 30.6 lb/s).

For single-well operation (Fig. 12, upper panel), the 5-1/2" tubing exhibits substantial pressure losses at the anticipated flow rates. At 32 bara cavern pressure and 10.9 kg/s, the wellhead pressure drops to approximately 20 bara (290 psia), representing a loss of roughly 35% of the zero-flow wellhead pressure. At the maximum flow rate of 13.9 kg/s, the 5-1/2" tubing becomes effectively choked. The 7" tubing performs markedly better, with wellhead pressure losses of approximately 1–2 bar (14.5–29.0 psi) across the operating range, maintaining wellhead pressures above 29 bara (420.6 psia) at all operating points.

For dual-well operation (Fig. 13, upper panel), the total flow is split approximately equally between HT04 and HT06, yielding per-well flow rates of 5.45–6.95 kg/s (12.0–15.3 lb/s). Under these conditions, the 7" tubing shows negligible losses (below 0.2 bar / 2.9 psi). Even using 5-1/2" tubing in each cavern results in acceptable wellhead pressure losses of approximately 0.3–0.5 bar (4.4–7.3 psi).

The lower panels of Figs. 12 and 13 plot both the pressure loss percentage and the energy loss percentage as a function of flow rate, computed at the minimum cavern pressure (32 bara) which represents the worst-case condition. Here, $p_{\mathrm{wh,ideal}}$ is defined as the wellhead pressure at zero flow (gravity-only static head), and the energy loss is evaluated using Eq. (9). A clear and consistent gap is visible between the two metrics across all flow rates: the energy loss is always lower than the pressure loss. This is because the pressure loss metric captures only the local drop from $p_{\mathrm{wh,ideal}}$ to $p_{\mathrm{wh,act}}$, whereas the energy loss is referenced to the full isothermal expansion path from wellhead pressure down to atmosphere. The denominator of the energy metric – $\ln\left(p_{\mathrm{wh,ideal}}/p_0\right)$ – is larger than the denominator implicit in the pressure ratio, which dilutes the fractional penalty.

For example, in single-well operation with the 5-1/2" tubing at the minimum operating flow rate of 10.9 kg/s, the pressure loss exceeds 10%, while the corresponding energy loss is approximately 6%. For the 7" tubing under the same conditions, the pressure loss is approximately 2–3%, while the energy loss remains below 1%. In dual-well operation, the gap narrows in absolute terms because both metrics are small, but the proportional relationship persists: the 5-1/2" tubing shows roughly 1.5% pressure loss versus approximately 0.5% energy loss at the design flow rates.

This distinction has practical implications for tubing selection. Conventional pressure-loss metrics, if used alone, overstate the true energetic penalty of well friction in the AirBattery discharge process and may lead to unnecessarily conservative tubing sizing. The energy-loss metric provides a more representative measure of the actual impact on plant round-trip efficiency.

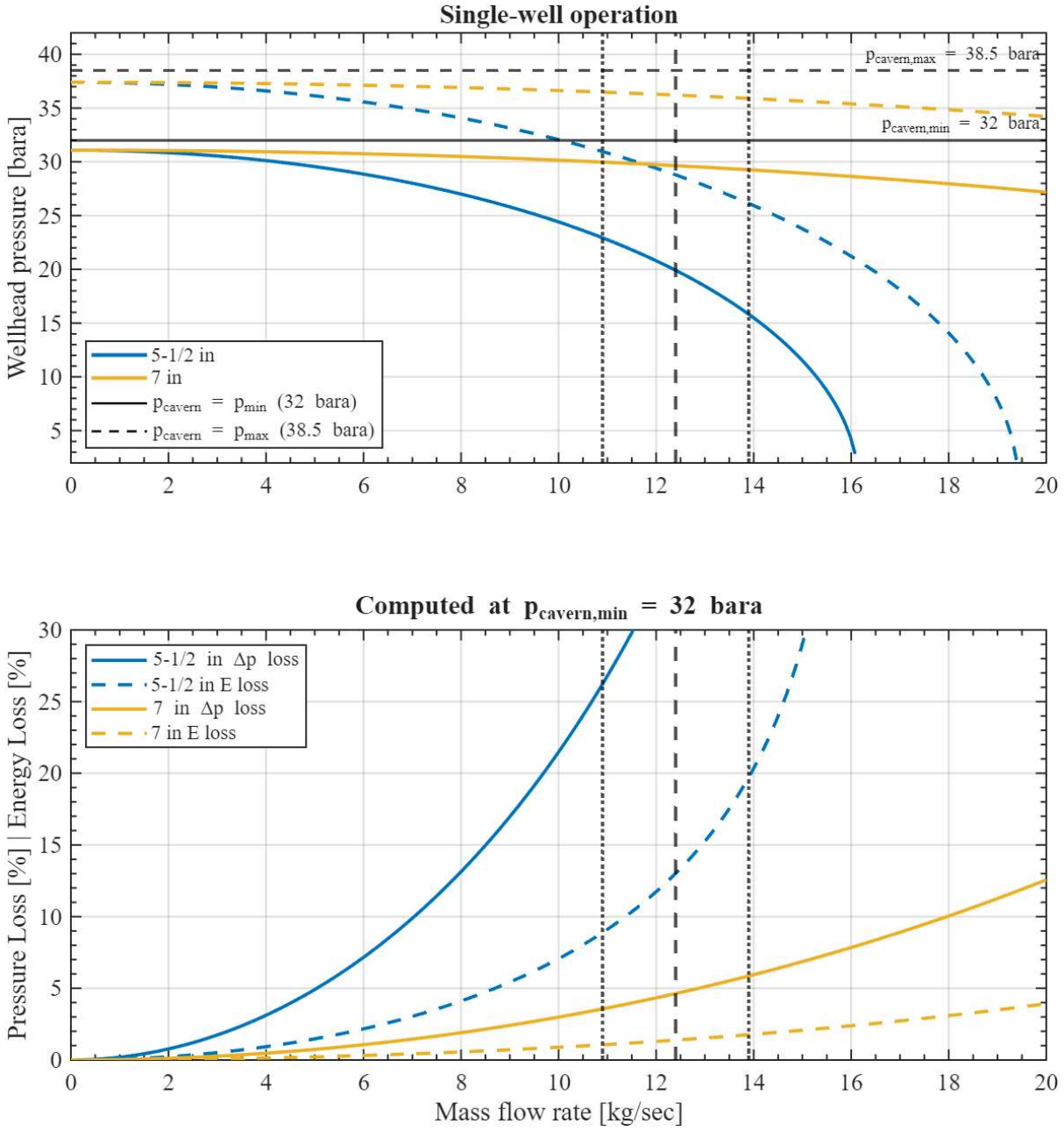

Figure 12. Single-well operation during discharge. Upper panel: Wellhead pressure as a function of mass flow rate for 5-1/2" and 7" tubing. Solid lines: $p_{cavern} = p_{min}$ (32 bara / 464.1 psia); dashed lines: $p_{cavern} = p_{max}$ (38.5 bara / 558.4 psia). Vertical markers indicate the expected operating flow rates at p_{min} (10.9 kg/s), average (12.4 kg/s), and p_{max} (13.9 kg/s). Lower panel: Pressure loss and energy loss as a percentage of the zero-flow (ideal) wellhead pressure and available work, respectively, computed at $p_{cavern,min} = 32$ bara. Solid lines: pressure loss (Eq. 8); dashed lines: energy loss (Eq. 9). Calculation parameters: $\bar{f} = 0.0165$, $T = 293.15$ K, $\theta = 90°$.

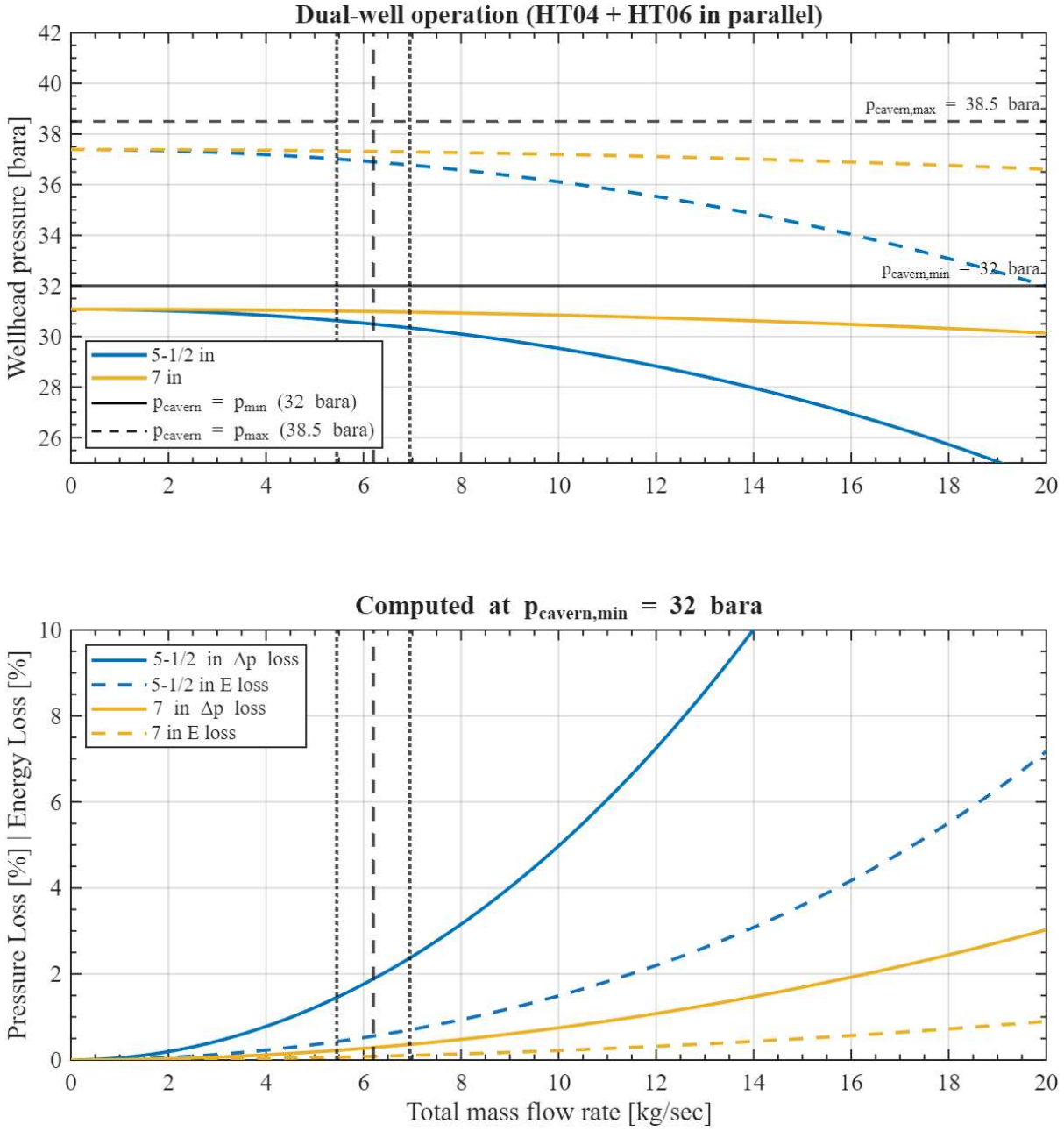

Figure 13. Dual-well operation (HT04 and HT06 in parallel) during discharge. The total flow is split equally between the two wells. Upper panel: Wellhead pressure as a function of total mass flow rate for 5-1/2" and 7" tubing. Same pressure cases and notation as Fig. 12. Lower panel: Pressure loss and energy loss percentages at $p_{cavern,min}$= 32 bara. Same loss definitions and calculation parameters as Fig. 12.

7. Debrining strategy of the HT04 and HT06 Caverns

The debrining concept for the Kistos Hilltop caverns HT04 and HT06 is based on displacing brine from the storage void by injecting compressed air. In the general arrangement, compressed air is introduced through the annular space between the outer tubing and the inner tubing, while brine is produced through the inner tubing, referred to as the debrining string.

A key constraint for the HT04-HT06 system is that the two caverns are considered likely to be hydraulically connected at a depth of approximately 292 meters (958 ft). As a result, they cannot be treated as independent storage volumes during debrining and must instead be operated simultaneously.

There are two possible operational concepts for such simultaneous debrining: (1) either both wells are used for debrining, (2) or one well is used for brine withdrawal while both wells are used for air injection. In both cases, the caverns behave as communicating vessels, so the brine level remains balanced between them and pressure differences must be avoided through well-aligned operation.

In the first concept, both wells are equipped for debrining. Compressed air from the AirBattery is injected into both caverns through the annular space, and brine is expelled through debrining strings in both wells and routed to the surface brine handling system. Because the caverns are connected, the liquid level in both caverns remains the same throughout the operation. This configuration therefore requires simultaneous and carefully coordinated debrining to prevent the development of a large differential pressure between the two caverns. Once the target debrining depth has been reached, the debrining strings are removed from the pressurized wells by snubbing.

The second concept uses only one well for debrining, while both wells are used for air injection. In this arrangement, compressed air is still introduced into both caverns, but brine is withdrawn through a single debrining string in one of the caverns. Because the caverns are connected, brine from the non-producing cavern flows toward the cavern equipped with the debrining string, thereby maintaining a common brine level in both caverns. An aspect of consideration in this concept is the anticipated brine flow through the connection between the caverns of half the debrining rate, so appx. 50 m^3/hr. It should be geomechanically checked if this is possible. Furthermore, the maximum debrining depth (at least for the cavern with no debrining string) in this concept is at the bottom of the connection, so at appx. 296 meters (971 ft).

8. Conclusions and Further Directions

Airengy continues to pursue scale up cost reductions and optimization through experiments at the demonstration site in Israel, as well as the engagement of experts such as turbomachinery design & procurement consultant, PhD. Gary Dyson.
For the Kistos CAPP project, Airengy and Kistos have procured Atkins Realis to further evaluate well design parameters and other cavern conversion considerations. Based on the evaluation results, Airengy and Kistos will determine the feasibility of the project. Provided that the project will be deemed feasible, Airengy and Kistos aim to complete the design and permitting of the first megawatt scale compressed air power plant by year end. A future development pathway is to extend the storage system beyond the initial HT04 and HT06 doublet by connecting additional caverns as they become available for compressed air, thereby increasing total storage volume and stored energy and enabling multi-cavern operation under the same pressure management.
During Q2 of 2026, Airengy also aims to announce an additional megawatt scale cavern connected facility within the E.U.
In addition, Airengy continues to develop its future pipeline through collaborations with cavern owners, such as an announced collaboration with SEFE Storage (Germany) related to its Jemgum site.

References

[1] IEA (2025). *Electricity 2026: Analysis and Forecast to 2030*. International Energy Agency, Paris.

[2] Colaluce, L. (2025, April 8). Solar curtailment surges by 97% in Germany in 2024 despite lower operational costs. *Strategic Energy Europe*. Accessed 17 March 2026.

[3] Wehrmann, B. (2024, April 9). Curtailing of renewable power increases in Germany in 2023 as re-dispatch costs recede. *Clean Energy Wire*. Accessed 17 March 2026.

[4] Agora Energiewende (2025). *Agorameter*, Version 4.1.2. Berlin. Chart view: "Power generation price," hourly data, 21 Oct 2024–31 Dec 2024. Accessed 14 October 2025.

[5] Murray, C. (2025, October 28). 'Terna is the big winner': Taking stock of Italy's MACSE auction. *Energy-Storage.news*.

[6] Baltay, A. (2025, October 8). MACSE Results: How developers delivered such low prices. *Modo Energy Research*.

[7] Radcliffe, J., Murrant, D., and Joshi, A. (2020). Energy Storage. Chapter 3 in *UK Roadmap for Energy Storage Research and Innovation*. University of Birmingham / Supergen Energy Storage Network+.

[8] Yogev, O., Koopmans, T., Joshua, T., and Tapiero, D. (2025). Isothermal Compressed Air Energy Storage (I-CAES) in Solution Mined Salt Cavern. Paper presented at the SMRI Spring 2025 Technical Conference, Wilhelmshaven, Germany, 28–29 April 2025.

[9] Koopmans, T., Faassen, C., Hoekstra, H., Krogh, S.J., and Brouard, B. (2022, September 26–27). CAES 2.0: Compressed air energy storage, the next generation. Paper presented at the SMRI Fall 2022 Technical Conference, Chester, United Kingdom.

[10] Aherne, S. and Kelly, J. (2013). Project CAES Larne – An Exploration Program for Compressed Air Energy Storage in Northern Ireland. Paper presented at the SMRI Fall 2013 Conference, Avignon, France.

[11] Cogen, A., and New York State Electric and Gas Corporation (NYSEG) (2012). *NYSEG Seneca Compressed Air Energy Storage (CAES) Demonstration Project: Final Report, Phase 1*. U.S. Department of Energy, Office of Electricity Delivery and Energy Reliability, Award DE-OE0000070. OSTI Report No. 1088675. Available at: https://www.osti.gov/biblio/1088675.

[12] Costley, J. and Cache Power Corp. (2025). Marguerite Lake Compressed Air Energy Storage Project. Alberta Major Projects Registry, Government of Alberta. Available at: https://majorprojects.alberta.ca/details/Marguerite-Lake-Compressed-Air-Energy-Storage/10922. Accessed 20 March 2026.

[13] Shaw, V. (2024, December 20). World's largest compressed air energy storage project breaks ground in China. *Energy Storage News*.

[14] Shaw, V. (2024, May 16). World's largest compressed air energy storage project comes online in China. *PV Magazine*.

[15] Maisch, M. (2025, January 10). World's largest compressed air energy storage facility commences full operation in China. *PV Magazine*.

[16] Crotogino, F., Mohmeyer, K.-U., and Scharf, R. (2001). Huntorf CAES: More than 20 years of successful operation. Paper presented at the SMRI Spring 2001 Meeting, Orlando, FL, USA.

[17] Enayati, A., Donadei, S., Izadi, S., and Krüger, U. (2025). Compressed Air Energy Storage (CAES) at Huntorf: Adapting to the Energy Transition. Paper presented at the SMRI Spring 2025 Technical Conference, Wilhelmshaven, Germany.

[18] Lux, K.-H. (2009). Design of salt caverns for the storage of natural gas, crude oil, and compressed air: Geomechanical aspects of construction, operation, and abandonment. In H.R. Thomas (Ed.), *Underground Storage of Natural Gas* (pp. 349–373). Springer.

[19] Brandt, M., Fabig, T., Kuperus, E., and Dirven, J. (2025). Fast multicyclic storage of hydrogen in salt caverns. Paper presented at the SMRI Spring 2025 Technical Conference, Wilhelmshaven, Germany.

[20] Horvath, L. and Schneider, G.-S. (2018, April). Update of SMRI's Compilation of Worldwide Salt Deposits and Salt Cavern Fields. Solution Mining Research Institute.

[21] GEOSTOCK (2026). *Augwind Hilltop CAES Conversion Assessment*. Report No. GK-HLTC1-STO-RPT-0001-C, Revision C, 24 February 2026. GEOSTOCK.

Appendix A

A.1 CAPP-BESS hybridization

To better understand how the batteries smooth the inherent oscillating power, we will examine their operation during charging and discharging. During discharge, an expanding compressed-air bubble drives water through the hydraulic turbines. As the compressed air bubble expands, its pressure drops over the cycle, which results in a decrease of the turbine instantaneous power. In order to supply constant power to the grid every cycle, a BESS is used to regulate cycle generated power fluctuations.

The control objective may be expressed by selecting a constant grid power supply setpoint $P_{\mathrm{grid,exp}}(t) = P_{\mathrm{set,dis}}$ equal to the cycle-average discharge power, enforcing

$$P_{\mathrm{grid,exp}}(t) = P_{\mathrm{set,dis}}(t) = P_{\mathrm{turb}}(t) + P_{\mathrm{BESS}}(t) \qquad (\mathrm{Eq.\,A1})$$

where $P_{\mathrm{turb}}(t)$ is the instantaneous turbine-generated power and $P_{\mathrm{BESS}}(t)$ is the battery power (positive when discharging to the grid, negative when charging).

Whenever $P_{\mathrm{turb}}(t) > P_{\mathrm{set,dis}}$, the excess turbine power charges the BESS, maintaining $P_{\mathrm{grid,exp}}(t)$ at P_{set}. Conversely, when $P_{\mathrm{turb}}(t) < P_{\mathrm{set,dis}}$, the BESS discharges to supply the missing power and reach $P_{\mathrm{set,dis}}$.

To maintain a repeatable operating mode with a near-constant state of charge (SOC), the cycle-integrated battery energy is kept at approximately zero (accounting for BESS charging and discharging efficiencies):

$$\int_{t_0}^{t_0+\tau} P_{\mathrm{BESS}}(t)\,dt \approx 0 \qquad (\mathrm{Eq.\,A2})$$

where τ is the cycle duration.

During charging phase, the instantaneous power demanded by the pumps and blowers fluctuates above and below the cycle-average demand. To maintain constant, steady power drawn from the grid, the BESS compensates for these variations by absorbing excess imported grid power when machine demand is below the average power and supplying the required additional power when machine demand exceeds the average power.

A constant grid power setpoint $P_{\mathrm{set,ch}}$ is selected as the cycle-average machine power demand, enforcing

$$P_{\mathrm{grid,imp}}(t) = P_{\mathrm{set,ch}}(t) = P_{\mathrm{pump}}(t) + P_{\mathrm{blower}}(t) + P_{\mathrm{BESS}}(t) \qquad (\mathrm{Eq.\,A3})$$

where $P_{\mathrm{pump}}(t) + P_{\mathrm{blower}}(t)$ is the instantaneous machines power demand, and $P_{\mathrm{BESS}}(t)$ is the battery power (positive when charging from the grid, negative when discharging to compensate the missing power to reach the $P_{\mathrm{set,ch}}$ of the pumps and the blowers). Analogous to Eq. (A2), the BESS SOC is kept at approximately zero.

Practically, this hybrid power-smoothing strategy enables the module rating to be defined by the average power of the machines rather than by the peak cyclic power and therefore reduces the required grid connection capacity.

Additionally, scaling up the CAPP with more AirBattery™ modules does not require additional batteries. When operating the AirBattery™ modules in a staggered arrangement, the same size BESS can be utilized for a much larger facility.

Fig. 14 illustrates the practical implementation of the BESS power-smoothing strategy described by Eqs. (A1)-(A2) across six consecutive discharge cycles recorded at the Yahel semi-commercial demonstration facility. During these tests, the air reservoir storage pressure (which dictates the cycle's initial pressure) dropped from 13.5 bar gauge to 8.5 bar gauge (195.8 psig to 123.3 psig), with each cycle lasting approximately 80 seconds.

As shown in Fig. 14(a), the instantaneous turbine power $P_{\mathrm{turb}}(t)$ follows a characteristic descending profile within each cycle, driven by the expanding air bubble and the corresponding drop in tank pressure. The turbine power peaks at approximately 175 kW during the first cycle and progressively decreases in subsequent cycles as the stored air pressure diminishes, reaching peak values of approximately 165, 155, 137, 122, and 113 kW in cycles 2 through 6, respectively. Despite this variation, the grid power $P_{\mathrm{grid,exp}}(t) = P_{\mathrm{set,dis}}(t)$ remains constant within each cycle, as enforced by Eq. (A1). The BESS absorbs the difference: during the early phase of each cycle, when $P_{\mathrm{turb}}(t) > P_{\mathrm{set,dis}}(t)$, the excess energy charges the battery (blue-shaded regions); during the later phase, when $P_{\mathrm{turb}}(t) < P_{\mathrm{set,dis}}$, the battery discharges to compensate for the power deficit (orange-shaded regions).

The grid setpoint for each cycle is not the simple arithmetic average of the turbine power, but rather an efficiency-corrected value that accounts for BESS round-trip losses ($\eta_{\mathrm{BESS,ch}} = \eta_{\mathrm{BESS,dis}} = 0.95$). This correction ensures that the cycle-integrated battery energy exchange satisfies the SOC-neutrality condition of Eq. (A1). The resulting setpoint is slightly lower than the simple average, reflecting the energy lost during each internal charge–discharge micro-cycle.

Fig. 14(b) confirms this behavior by displaying the cumulative BESS stored energy over the full test duration. Within each cycle, the stored energy first increases as excess turbine power is absorbed and then decreases as the battery compensates for the turbine deficit. At the end of each cycle, the BESS state of energy returns to approximately zero ($\Delta E_{\mathrm{BESS}} \approx 0$), demonstrating repeatable SOC-neutral operation without progressive battery depletion or overcharge.

From a system design perspective, this hybrid strategy decouples the grid connection rating from the peak cyclic turbine power. The grid interface is sized according to the cycle-average power rather than the instantaneous peak, reducing connection capacity requirements and associated infrastructure costs. Furthermore, as noted above, scaling the CAPP by adding AirBattery modules in a staggered arrangement does not require proportional BESS scaling, since the phase offset between modules inherently reduces the aggregate power fluctuation seen by a shared battery.

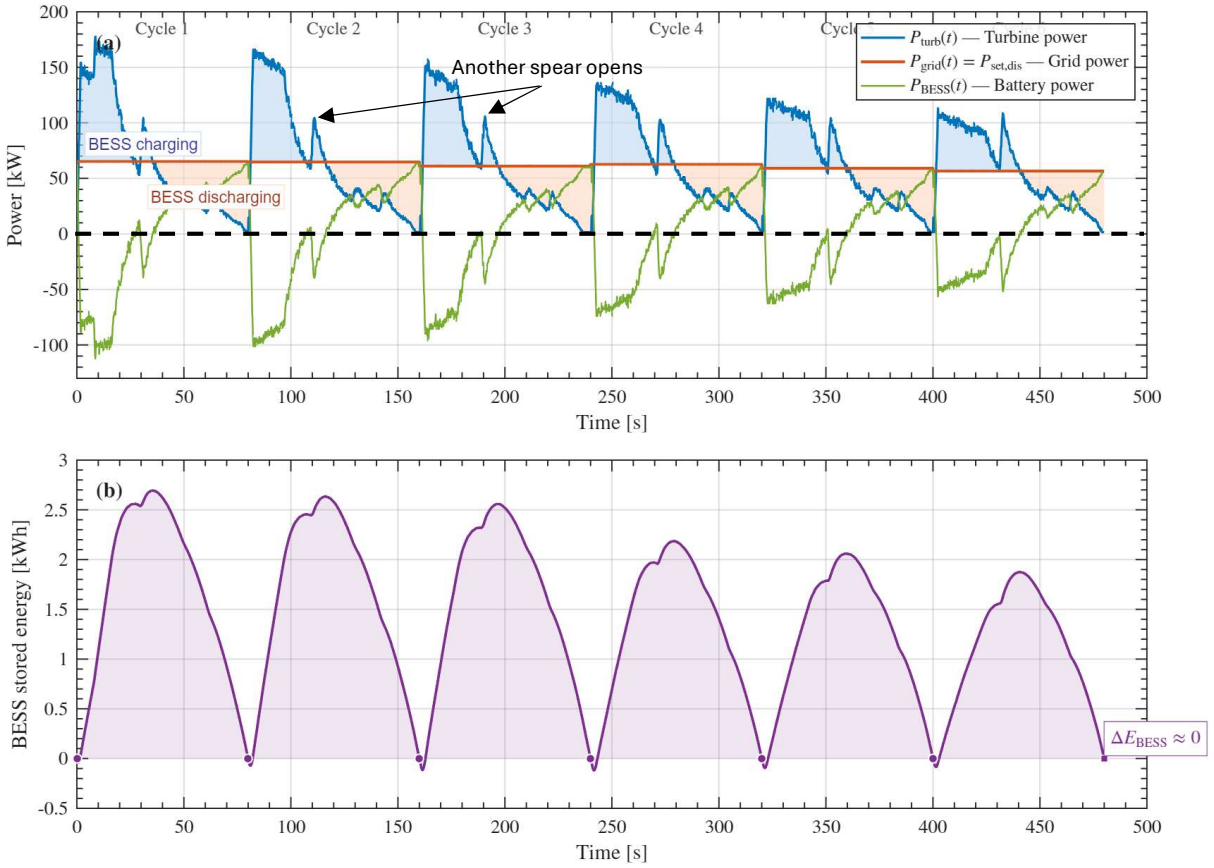

Figure 14. (Extension of Fig. 7) - BESS hybridization across six consecutive AirBattery discharge cycles at the Yahel semi-commercial facility.

Appendix B

B.1 Minimum Operating Pressure

The minimum operating pressure in the HT04 and HT06 cavern system is estimated to be around 31 bar gauge (450 psig). This pressure corresponds to the saturated brine pressure at the lower level of the HT06 cavern roof, which is 260 meters (853 ft) deep. This minimum pressure is considered sufficient to ensure the stability of the cavern roofs and pillars.

Fig. 15 shows a simplified and conservative cavern field layout that can be analyzed to evaluate the average stress on the salt pillars. The vertical stress in the salt pillars (orange area) is estimated at 15 MPa (2,176 psi) for a cavern pressure of 31 bar gauge (450 psig). Using the Hilltop salt dilation criterion (with a confining pressure of 31 bar gauge (450 psig) corresponding to cavern minimum pressure), the dilation index is estimated at 0.5, corresponding to a safety factor of 2. However, the fatigue behavior of the rock and the long-term degradation of the claystone layers have not been accounted for.

For completeness, the vertical stress at the 320 meters (1,050 ft) depth (cavern bottom level) before caverns leaching is evaluated as

$$\sigma_v = 200\ [m] \times 0.025 \left[\frac{MPa}{m}\right] + 120[m] \times 0.022 \left[\frac{MPa}{m}\right] \approx 7.6[MPa] \qquad \text{(Eq. B. 1)}$$

and the extension of the studied zone is

$$L = 3 \times 130[m] + 2 \times 16[m] + 2 \times 8[m] = 438[m] \qquad \text{(Eq. B. 2)}$$

as shown on Fig. 15.

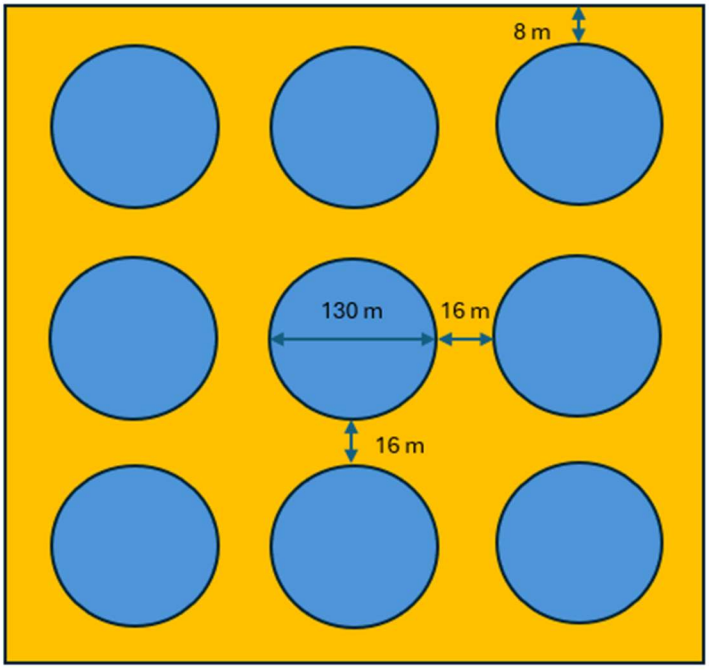

Figure 15. Simplified Hilltop caverns layout

The stability of the cavern roof can be assessed using the simplified “classical plate theory” approach. In this method, the thickness of the salt layer above the cavern is checked to determine the safety factor against tensile failure at the roof. Using this approach, the minimum thickness of the salt layer above the cavern should be approximately 70% of the cavern radius for a minimum operating pressure of 31 bar gauge (450 psig).

Considering an average cavern radius of 53 meters (174 ft) – calculated between 40 meters (131 ft) at the roof and 65 meters (213 ft) at the bottom – the minimum required salt thickness is estimated at 37 meters (121 ft). The actual salt thickness above the caverns is between 41 and 45 meters (135 and 148 ft) on the wells, which meets this requirement. This approach is conservative under the condition that either the salt plate above the roof is homogeneous or that any alternative layers of insoluble beds and salt between the cavern roof and the rockhead remain fully bonded. No additional safety margin is taken at this stage.

B.2 Maximum Operating Pressure

The maximum cavern pressure is set to prevent the infiltration of gas or air into the surrounding rock mass and adjacent caverns. This limit is based on the effective least compressive stress around the cavern and is defined as the pressure at which the effective tangential stress at the cavern roof becomes tensile, indicating the potential onset of air migration from HT04 and HT06.

The gas infiltration criterion dictates that the gas pressure in the cavern must remain lower than the compressive hoop stress at the cavern roof. Using the analytical approach adopted for cylindrical caverns, the maximum allowable pressure may be expressed through an equivalent maximum pressure gradient in the formation.

Taking a far-field lithostatic stress gradient of 0.022 MPa/m (0.97 psi/ft) and a brine pressure gradient of 0.012 MPa/m (0.53 psi/ft), the maximum pressure gradient is estimated as:

$$\left(\frac{dp_{\max}}{dz}\right) = 0.0153 \left[\frac{MPa}{m}\right] \qquad \text{(Eq. B. 3)}$$

For the case of HT04, the cavern roof is at 245 meters (804 ft), the maximum pressure is evaluated as:

$$p_{\max}(z) = 0.0153 \left[\frac{MPa}{m}\right] \times 245[m] = 3.75[MPa] = 37.5[bar] \qquad \text{(Eq. B. 4)}$$

Accordingly, the maximum air pressure at the cavern roof is taken as 37.5 bar gauge (544 psig), consistent with the pressure table used in the assessment.

Appendix C

C.1 Analytical Model for Isothermal Compressible Flow in Inclined Pipelines

This section derives an analytical equation to determine the pressure distribution along an inclined pipeline under steady-state air flow, subject to the following primary assumptions:

Assumption 1: The flow remains isothermal, maintaining a constant temperature along the pipeline.

Assumption 2: The fluid is compressible, with density varying as a function of pressure.

Assumption 3: The fluid exhibits ideal gas behavior.

Assumption 4: The pipeline maintains a constant internal diameter, and the combined pressure losses from wall friction and localized fittings are modeled utilizing the Darcy-Weisbach formulation.

The ultimate objective of this derivation is to calculate the outlet pressure p_{out} as a function of the inlet pressure p_{in} across an inclined pipeline segment of length L, accounting for friction losses, localized losses from fittings (e.g., valves, elbows), and gravitational static head effects.

The derivation proceeds from the fundamental differential head-loss expression. Integrating the Darcy-Weisbach framework for isothermal, compressible flow within vertical pipelines, the governing differential equation for head loss is formulated as:

$$dH = \left[-\frac{v^2}{2\mathrm{g}}\left(\frac{\bar{f}}{d_{in}} + \frac{K_\Sigma}{L}\right) - \sin\theta\right] dx \qquad (\mathrm{Eq.\,C1})$$

Where dH denotes the differential head loss, dx represents the differential pipe length, d_{in} is the internal pipe diameter, v is the fluid velocity, g is the gravitational acceleration, $\bar{f}$ represents the average friction factor, K_Σ denotes the cumulative loss coefficient for fittings distributed along length L, and θ establishes the flow direction angle convention according to Fig. 16 ($\theta = 90°$ for vertical up-flow, $\theta = 270°$ or $-90°$ for vertical down-flow).

Physically, the term containing v^2 characterizes the energy losses related to friction along pipeline and fittings, whereas the $\sin\theta$ term captures the gravitational contribution, adopting a value of +1 or -1 for vertical up-flow or down-flow configurations, respectively, depending on the flow direction angle θ.

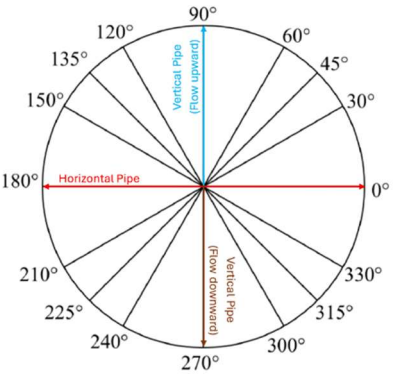

Figure 16. Definition of the pipe inclination angle and flow-direction convention used in the pressure-loss model, with 0° and 180° representing a horizontal pipe, 90° representing a vertical pipe with upward flow, and 270° representing a vertical pipe with downward flow.

To relate pressure variations to head variations over a differential pipe segment, the mechanical-energy balance yields the following relationship between the differential pressure change dp and the differential head change dH:

$$dp = \rho(p)\,\mathrm{g}\,dH \qquad \text{(Eq. C2)}$$

Under the assumption of isothermal ideal gas behavior, fluid density ρ relates to pressure p as follows, which can be rearranged to express density directly:

$$p = \rho R_{\mathrm{air}} T \qquad \text{(Eq. C3)}$$

Rearranging gives:

$$\rho = \frac{p}{R_{\mathrm{air}} T} \qquad \text{(Eq. C4)}$$

Substituting the ideal-gas density expression into the mechanical-energy balance provides:

$$dp = \frac{p}{R_{\mathrm{air}} T}\,\mathrm{g}\,dH \qquad \text{(Eq. C5)}$$

Rearranging the expression to isolate the pressure-dependent variables establishes the necessary form for subsequent integration:

$$dH = \left(\frac{R_{\mathrm{air}} T}{\mathrm{g}}\right)\frac{1}{p}dp \qquad \text{(Eq. C6)}$$

Substituting this differential head expression back into the expanded Darcy-Weisbach relation reformulates the governing equation strictly in terms of pressure p and spatial coordinate x:

$$\frac{R_{\mathrm{air}} T}{\mathrm{g}p}dp = \left[-\frac{v^2}{2\mathrm{g}}\left(\frac{\bar{f}}{d_{in}} + \frac{K_{\Sigma}}{L}\right) - \sin\theta\right]dx \qquad \text{(Eq. C7)}$$

Assuming steady-state conditions, the mass flow rate $\dot{m}_{\mathrm{air}}$ remains constant along the longitudinal axis of the pipeline:

$$\dot{m}_{\mathrm{air}} = \rho v A_c \qquad \text{(Eq. C8)}$$

Recalling the pressure dependency of gas density from the ideal gas law, the mass flow rate equation is modified accordingly:

$$\rho = \frac{p}{R_{\mathrm{air}} T} \qquad \text{(Eq. C9)}$$

Replace ρ in the mass flow rate term, we get:

$$\dot{m}_{\mathrm{air}} = \frac{p}{R_{\mathrm{air}} T} v A_c \qquad \text{(Eq. C10)}$$

Isolating the local velocity v yields a pressure-dependent function, which is subsequently squared to align with the head-loss formulation:

$$v = \frac{\dot{m}_{\mathrm{air}} R_{\mathrm{air}} T}{p A_c} \qquad \text{(Eq. C11)}$$

Squaring both sides gives:

$$v^2 = \frac{\dot{m}_{\mathrm{air}}^2 {R_{\mathrm{air}}}^2 T^2}{p^2 A_c^2} \qquad \text{(Eq. C12)}$$

Substituting the squared velocity term into the modified Darcy-Weisbach equation eliminates the velocity variable, reformulating the expression entirely in terms of mass flow rate $\dot{m}$ and pressure p:

$$\frac{R_{\text{air}}T}{\text{g}p}dp = \left[-\frac{\dot{m}_{\text{air}}{}^2 R_{\text{air}}{}^2 T^2}{2\text{g}p^2 A_c^2}\left(\frac{\bar{f}}{d_{in}} + \frac{K_\Sigma}{L}\right) - \sin\theta\right]dx \qquad \text{(Eq. C13)}$$

$$dp = \left[-\frac{\dot{m}_{\text{air}}{}^2 R_{\text{air}} T}{2pA_c^2}\left(\frac{\bar{f}}{d_{in}} + \frac{K_\Sigma}{L}\right) - \frac{\text{g}p}{R_{\text{air}}T}\sin\theta\right]dx \qquad \text{(Eq. C14)}$$

Given the constant internal diameter of the pipeline, the cross-sectional area A_c remains uniform, yielding the following squared relationship:

$$A_c = \frac{\pi d_{in}{}^2}{4} \qquad \text{(Eq. C15)}$$

Squaring both sides gives:

$$A_c^2 = \frac{\pi^2 d_{in}{}^4}{16} \qquad \text{(Eq. C16)}$$

Incorporating the geometric area expression into the primary differential equation isolates the unknown pressure profile $p(x)$ against a set of known operational constants:

$$dp = \left[-\frac{8\dot{m}_{\text{air}}{}^2 R_{\text{air}} T}{p\pi^2 d_{in}{}^4}\left(\frac{\bar{f}}{d_{in}} + \frac{K_\Sigma}{L}\right) - \frac{\text{g}p}{R_{\text{air}}T}\sin\theta\right]dx \qquad \text{(Eq. C17)}$$

$$dp = \left[-\frac{8\dot{m}_{\text{air}}{}^2 R_{\text{air}} T}{p\pi^2 d_{in}{}^5}\bar{f} - \frac{8\dot{m}_{\text{air}}{}^2 R_{\text{air}} T}{p\pi^2 d_{in}{}^4 L}K_\Sigma - \frac{\text{g}p}{R_{\text{air}}T}\sin\theta\right]dx \qquad \text{(Eq. C18)}$$

To streamline the analytical solution, the physical constants are aggregated into two distinct coefficients: Coefficient a consolidates the mechanical energy losses induced by wall friction and fittings, whereas coefficient b isolates the hydrostatic forces governed by gravity, fluid temperature, and pipeline inclination.

$$a = -\frac{8\dot{m}_{\text{air}}{}^2 R_{\text{air}} T}{\pi^2 d_{in}{}^4}\left(\frac{\bar{f}}{d_{in}} + \frac{K_\Sigma}{L}\right) \qquad \text{(Eq. C19)}, \qquad b = -\frac{\text{g}}{R_{\text{air}}T}\sin\theta \qquad \text{(Eq. C20)}$$

Applying these coefficient definitions yields a simplified differential formulation, which can be algebraically rearranged into a standard integrable form:

$$dp = \left(\frac{a}{p} + bp\right)dx \qquad \text{(Eq. C21)}$$

Rearranging the integrand gives:

$$dp = \left(\frac{a + bp^2}{p}\right)dx \qquad \text{(Eq. C22)}$$

$$\frac{p}{a + bp^2}dp = dx \qquad \text{(Eq. C23)}$$

Integrating the governing equation over the spatial domain from the pipeline inlet ($x = 0$, evaluating at pressure p_{in}) to the outlet ($x = L$, evaluating at pressure p_{out}) provides:

$$\int_{p_{\text{in}}}^{p_{\text{out}}} \frac{p}{a + bp^2}\, dp = \int_0^L 1\, dx \qquad \text{(Eq. C24)}$$

$$\frac{\ln(a + bp^2)}{2b}\Big|_{p_{\text{in}}}^{p_{\text{out}}} = x\Big|_0^L \qquad \text{(Eq. C25)}$$

$$\frac{\ln(a + bp_{\text{out}}^2) - \ln(a + bp_{\text{in}}^2)}{2b} = L \qquad \text{(Eq. C26)}$$

$$\ln\left(\frac{a + bp_{\text{out}}^2}{a + bp_{\text{in}}^2}\right) = 2bL \qquad \text{(Eq. C27)}$$

$$\frac{a + bp_{\text{out}}^2}{a + bp_{\text{in}}^2} = e^{2bL} \qquad \text{(Eq. C28)}$$

$$a + bp_{\text{out}}^2 = (a + bp_{\text{in}}^2)e^{2bL} \qquad \text{(Eq. C29)}$$

$$p_{\text{out}}^2 = \frac{(a + bp_{\text{in}}^2)e^{2b} - a}{b} \qquad \text{(Eq. C30)}$$

$$p_{\text{out}} = \sqrt{\frac{(a + bp_{\text{in}}^2)e^{2bL} - a}{b}} \qquad \text{(Eq. C31)}$$

$$p_{\text{out}} = \sqrt{\frac{(a + bp_{\text{in}}^2)e^{2b}}{b} - \frac{a}{b}} \qquad \text{(Eq. C32)}$$

Isolating the outlet pressure p_{out} generates the definitive closed-form analytical solution for the complete vertical pipeline segment, which may also be expressed in the following equivalent formats:

$$p_{\text{out}} = \sqrt{\left(\frac{a}{b} + p_{\text{in}}^2\right)e^{2bL} - \frac{a}{b}} \qquad \text{(Eq. C33)}$$

The same integrated result can be written in an equivalent form:

$$p_{\text{out}} = \sqrt{\frac{a}{b}(e^{2bL} - 1) + e^{2b}\ p_{\text{in}}^2} \qquad \text{(Eq. C34)}$$

Consequently, the total pressure differential across the inclined segment is defined as:

$$\Delta p_{\text{total}} = p_{\text{out}} - p_{\text{in}} = \sqrt{\left(\frac{a}{b} + p_{\text{in}}^2\right)e^{2bL} - \frac{a}{b}} - p_{\text{in}} \qquad \text{(Eq. C35)}$$

For analytical clarity, the total pressure change may be conceptualized through superposition, comprising two distinct components: a primary component driven by friction and fittings, and a secondary component governed by gravitational static head.

Evaluating the frictional and localized loss component independently, applicable to horizontal pipeline segments where gravitational effects are negligible ($b = 0$), yields the following isolated outlet pressure and corresponding pressure drop:

$$b = 0 \qquad \text{(Eq. C36)}$$

$$\int_{p_{\text{in}}}^{p_{\text{out}}} \frac{p}{a}\, dp = \int_{0}^{L} 1\, dx \qquad \text{(Eq. C37)}$$

$$p_{\text{out,loss}} = \sqrt{p_{\text{in}}^2 + 2La} \qquad \text{(Eq. C38)}$$

The resulting pressure loss attributable strictly to frictional and localized resistance is expressed as:

$$\Delta p_{\text{loss}} = p_{\text{out,loss}} - p_{\text{in}} = \sqrt{p_{\text{in}}^2 + 2La} - p_{\text{in}} \qquad \text{(Eq. C39)}$$

Conversely, evaluating the static-head component independently, assuming idealized, frictionless flow without localized restrictions ($a = 0$), provides the elevation-driven outlet pressure and pressure differential:

$$a = 0 \qquad \text{(Eq. C40)}$$

$$\int_{p_{\text{in}}}^{p_{\text{out}}} \frac{1}{b} p\, dp = \int_{0}^{L} 1\, dx \qquad \text{(Eq. C41)}$$

$$p_{\text{out,gravity}} = p_{\text{in}} e^{bL} \qquad \text{(Eq. C42)}$$

The isolated pressure loss induced by hydrostatic elevation changes is therefore given by:

$$\Delta p_{\text{gravity}} = p_{2_{\text{gravity}}} - p_{\text{in}} = p_{\text{in}} e^{bL} - p_{\text{in}} = p_{\text{in}}(e^{bL} - 1) \qquad \text{(Eq. C43)}$$

Appendix D

D.1 Distinction between pressure loss and energy loss

Pressure loss and energy loss are related quantities, but they are not identical and should not be interpreted interchangeably. Consider one AirBattery discharge cycle in which a single air bubble rises from the cavern roof to the wellhead and then enters a water-filled surface tank. Let $p_{\mathrm{wh,ideal}}$ denote the bubble pressure at the wellhead in the ideal case without frictional and localized losses, and let $p_{\mathrm{wh,act}}$ denote the actual wellhead pressure when those losses are present, with $p_{\mathrm{wh,ideal}} > p_{\mathrm{wh,act}}$. Because water in the tank is incompressible, the bubble immediately raises the tank pressure to the corresponding wellhead pressure. For the same delivered bubble mass and under the isothermal assumption,

$$p_{\mathrm{wh,ideal}} V_{\mathrm{ideal}} = p_{\mathrm{wh,act}} V_{\mathrm{actual}} = C = m_{\mathrm{air,bubble}} R_{\mathrm{air}} T \qquad \text{(Eq. D1)}$$

where V_{ideal} and V_{actual} are the volumes occupied by the air bubble at the valve-closure point inside the tank for the ideal and actual cases, respectively, C is constant for that bubble across all expansion cycles, and $m_{\mathrm{air,bubble}}$ is the transported bubble mass.

The useful work delivered to the hydraulic turbine must be evaluated against the atmospheric backpressure p_0. During the open phase, while the cavern valve remains open and the tank pressure is held constant at p_{j} ($\mathrm{j} = \mathrm{ideal, actual}$), the useful work is

$$W_{\mathrm{open,j}} = \int_0^{V_{\mathrm{j}}} (p_{\mathrm{j}} - p_0)\, dV \qquad \text{(Eq. D2)}$$

hence

$$W_{\mathrm{open,j}} = (p_{\mathrm{j}} - p_0) V_{\mathrm{j}} = C\left(1 - \frac{p_0}{p_{\mathrm{j}}}\right) \qquad \text{(Eq. D3)}$$

After the valve closes, the same bubble undergoes closed isothermal expansion from V_{j} to V_{f} (the final expanded volume and $V_{\mathrm{f}} \gg V_{\mathrm{actual}} > V_{\mathrm{ideal}}$). For this process, pressure varies with volume as

$$p(V) = \frac{C}{V} \qquad \text{(Eq. D4)}$$

The useful work of the closed phase is therefore

$$W_{\mathrm{closed,j}} = \int_{V_{\mathrm{j}}}^{V_{\mathrm{f}}} \left(\frac{C}{V} - p_0\right) dV \qquad \text{(Eq. D5)}$$

$$W_{\mathrm{closed,j}} = C \ln\left(\frac{V_{\mathrm{f}}}{V_{\mathrm{j}}}\right) - p_0 (V_{\mathrm{f}} - V_{\mathrm{j}}) \qquad \text{(Eq. D6)}$$

Substituting $V_{\mathrm{j}} = C/p_{\mathrm{j}}$,

$$W_{\mathrm{closed,j}} = C \ln\left(\frac{p_{\mathrm{j}} V_{\mathrm{f}}}{C}\right) - p_0 \left(V_{\mathrm{f}} - \frac{C}{p_{\mathrm{j}}}\right) \qquad \text{(Eq. D7)}$$

and the total useful work per air bubble becomes

$$W_{\mathrm{j}} = C\left[1 + \ln\left(\frac{p_{\mathrm{j}} V_{\mathrm{f}}}{C}\right)\right] - p_0 V_{\mathrm{f}} \qquad \text{(Eq. D8)}$$

The percentage pressure loss between the cavern roof and the wellhead is simply

$$\Delta p_{\mathrm{loss}}[\%] = 100 \cdot \frac{p_{\mathrm{wh,ideal}} - p_{\mathrm{wh,act}}}{p_{\mathrm{wh,ideal}}} \qquad \text{(Eq. D9)}$$

By contrast, the percentage loss in available useful work, referenced to the no-loss case, is

$$E_{\mathrm{loss}}[\%] = 100 \cdot \frac{W_{\mathrm{ideal}} - W_{\mathrm{act}}}{W_{\mathrm{ideal}}} = 100 \cdot \frac{\ln\left(p_{\mathrm{wh,ideal}}/p_{\mathrm{wh,act}}\right)}{1 + \ln\left(p_{\mathrm{wh,ideal}} V_{\mathrm{f}}/C\right) - p_0 V_{\mathrm{f}}/C} \qquad \text{(Eq. D10)}$$

If the closed expansion continues until the bubble pressure reaches atmospheric, such that $V_{\mathrm{f}} \cdot p_0 = C$, Eq. (D10) simplifies to

$$E_{\mathrm{loss}}[\%] = 100 \cdot \frac{\ln\left(\frac{p_{\mathrm{wh,ideal}}}{p_{\mathrm{wh,act}}}\right)}{\ln\left(\frac{p_{\mathrm{wh,ideal}}}{p_0}\right)} \qquad \text{(Eq. D11)}$$

All pressures in this section are absolute. These expressions show clearly why pressure loss and energy loss cannot be used interchangeably. The pressure metric depends only on the local drop from $p_{\mathrm{wh,ideal}}$ to $p_{\mathrm{wh,act}}$, whereas the energy metric is referenced to the full expansion path from wellhead pressure down to atmosphere and is therefore smaller. Consequently, pressure-loss percentages systematically overstate the true energetic penalty of well and tubing losses in the AirBattery discharge process.